POLITECNICO DI TORINO
Repository ISTITUZIONALE

Viscoelasticity of suspension of red blood cells under oscillatory shear flow

(Article begins on next page)

05 February 2025

Article

Viscoelasticity of suspension of red blood cells under oscillatory shear flow

Naoki Takeishi,[1, 2, a)] Marco Edoardo Rosti,[3] Naoto Yokoyama,[4] and Luca Brandt[5, 6, 7]

[1)]*Faculty of Mechanical Engineering, Kyoto Institute of Technology, Goshokaido-cho, Matsugasaki, Sakyo-ku, Kyoto, 606-8585, Japan*

[2)]*Graduate School of Engineering Science, Osaka University, 1-3 Machikaneyama, Toyonaka, Osaka 560-8531, Japan*

[3)]*Complex Fluids and Flows Unit, Okinawa Institute of Science and Technology Graduate University, 1919-1 Tancha, Onna-son, Okinawa 904-0495, Japan*

[4)]*Department of Mechanical Engineering, Tokyo Denki University, 5 Senju-Asahi, Adachi, Tokyo, 120-8551, Japan*

[5)]*FLOW, Department of Engineering Mechanics, Royal Institute of Technology (KTH), SE 100 44 Stockholm, Sweden*

[6)]*Department of Energy and Process Engineering, Norwegian University of Science and Technology (NTNU), Trondheim, Norway*

[7)]*Department of Environmental, Land, and Infrastructure Engineering, Politecnico di Torino, Corso Duca degli Abruzzi 24, 10129, Turin, Italy*

(Dated: 19 March 2024)

We present a numerical analysis of the rheology of a suspension of red blood cells (RBCs) for different volume fractions in a wall-bounded, effectively inertialess, small amplitude oscillatory shear (SAOS) flow for a wide range of applied frequencies. The RBCs are modeled as biconcave capsules, whose membrane is an isotropic and hyperelastic material following the Skalak constitutive law. The frequency-dependent viscoelasticity in the bulk suspension is quantified by the complex viscosity, defined by the amplitude of the particle shear stress and the phase difference between the stress and shear. SAOS flow basically impedes the deformation of individual RBCs as well as the magnitude of fluid-membrane interactions, resulting in a lower specific viscosity and first and second normal stress differences than in steady shear flow. Although it is known that the RBC deformation alone is sufficient to give rise to shear-thinning, our results show that the complex viscosity weakly depends on the frequency-modulated deformations or orientations of individual RBCs, but rather depends on combinations of the frequency-dependent amplitude and phase difference. The effect of the viscosity ratio between the cytoplasm and plasma and of the capillary number are also assessed.

I. INTRODUCTION

Human blood is a dense suspension consisting of 55% plasma (which is typically assumed Newtonian fluid), and 45% blood cells, with over 98% of the cells being red blood cells (RBCs), which are non-spherical deformable particles. The study of the hydrodynamic interactions between individual RBCs and their consequent deformation is of fundamental importance for the bulk rheology of human blood, because these are responsible for the non-Newtonian behavior of the suspension, the well-known shear-thinning behavior[1–4]. The RBC deformability highly complicates the suspension rheology, being key to determining the haemorheology. Indeed, the shear-thinning character of the blood disappears when RBCs are hardened[1,2], with the blood suspension exhibiting an almost Newtonian behavior and higher viscosity compared to a suspension of normal RBCs. Several researchers have attempted to relate the rheological nature of the blood to the dynamics of RBCs, starting from experimental observations of the individual cell behaviors under controlled flows, usually simple steady shear flows, e.g., in Refs. 5–8. More recently, numerical simulations have been also adopted to investigate the motion of RBCs at different steady shear rates; in particular, it was found that RBCs experience transitions from rolling/tumbling motions to kayaking (or oscillating/swinging) and swinging, following tank-treading motions as the shear rate increases for a wide range of ratios between the internal and external fluid viscosity ($\lambda = 0.1$–10)[8–11]. Lanotte *et al.*[8] further showed that tank-treading does occur for low viscosity contrasts ($\lambda \approx 0.25$), but is suppressed at high viscosity contrasts, when rotating multilobar shapes appear instead. The behavior of cells in flow, including vesicles, which are also enveloped by lipid bilayers, from individual dynamics to rheology was outlined in Ref. 12. In our recent numerical analysis, we have related the aforementioned single-cell behavior to the bulk suspension rheology, and successfully demonstrated the shear-thinning character of blood flow examining the cellular-scale dynamics under steady shear[11].

In real human blood, RBCs are constantly under mechanical stimulation from the plasma flow due to the heart beat (≈ 1 Hz) and from the vessel walls in various organs. It is also known that RBCs travel in the body as an oxygen carrier, and easily alter their shapes to pass through 3-to-4 μm capillaries[13], where the upper limit of shear stress in the human circulatory system has been estimated to be 15 Pa[14]. However, when they travel through artificial blood pumps, the cells may experience much higher shear stresses, up to 1000 Pa[15]. From a physiological viewpoint, the relationship between the deformation, as a mechanical response to oscillatory loading, and the oxygen transport, as a biological function, is therefore of great interest, and several studies have shed some light on this[16–18]. The rheological description of blood under oscillatory flow is thus of fundamental importance not only for

[a)]Authors to whom correspondence should be addressed: ntakeishi@kit.ac.jp

a physiological understanding but also in the design of novel artificial blood pumps that minimize mechanical stimuli that may cause the rupture of RBCs, the so-called hemolysis. Using a capsule model consisting of a Newtonian fluid enclosed by a thin elastic membrane, Matsunaga et al. [19] demonstrated that frequency-dependent deformations of a single spherical capsule become evident for high shear rates and large values of the viscosity contrast between the internal and external fluids. However, it is still unknown whether this knowledge can be used for suspensions of RBCs. The first question in this study is, therefore, whether the cell deformation is reduced or enhanced by varying the oscillatory frequency. Although the recovery of RBCs under oscillatory flow has been investigated in the past via experimental observations[20–22], and model analysis[23–26], much is still unknown, especially in relation to the bulk suspension rheology and to the dynamical viscoelasticity of suspensions of RBCs under oscillatory shear flow. Hence, our second question is how the viscoelastic character of the suspension of RBCs differs in an oscillatory shear flow with respect to the steady case.

The linear mechanical response of soft materials to weak oscillatory shear strain $\gamma(t)$ is generally frequency dependent and viscoelastic, so that the oscillatory stress τ can be expressed with the help of a complex shear modulus G^*: $\tau(t) = G^*\gamma(t)$[27,28]. The complex modulus G^* can be decomposed into its two components, $G^* = G' + iG''$, where the real part G' is the storage modulus representing the elastic component of the stress, and the imaginary part G'' is the loss modulus representing the viscous dissipative part[27,28]. Traditional (macroscopic) rheometers enable direct mechanical measurements of the frequency dependent G^*. To cite few relevant examples, Mason and Weitz[29] extracted the rheological properties from the thermal motion of colloidal probes embedded within the material, whereas Wagner[30] and Lionberger and Russel[31] calculated G' at high frequency in hard-sphere dispersions from theory, and compared the results to the experiments by Shikata and Pearson[32]. Although numerical simulations allow us to quantify the dynamical viscoelasticity by calculating the complex moduli, the analysis of deformable particle suspensions is still a challenge because the hydrodynamic coupling among the particles, their deformation and the solvent motion must all be taken into account[30,31].

As regards the role of deformability, Frohlich and Sack[33] were the first to investigate a suspension of Hookean elastic spheres and reported a linearized Oldroyd-type constitutive equation derived to relate the macroscopic extensional stress and the strain rate. Oldroyd[34] reported that a suspension of Newtonian droplets in another Newtonian liquid exhibits viscoelastic behavior with an Oldroyd-type constitutive relation. The rheological behavior of such suspensions is similar to that of a suspension of elastic particles in a Newtonian fluid. Based on the coupled solutions for the flow field around the particle and the deformation of the particle, both analytical and numerical approaches have been applied to investigate the dilute suspension rheology, especially under steady shear flow[35–38]. Among others, Goddard and Miller[36] derived constitutive equations for the rheological behavior of a suspension of slightly deformed viscoelastic spheres in the dilute

limit. Misbah[37] derived equations which describe the vesicle orientation in the flow and its shape evolution, and outlined a rheological law for a dilute vesicle suspension. Along with these analytical and numerical studies, recent computer simulation approaches have been successfully used to investigate rheological properties of a dilute and semi-dilute suspension of deformable particles in steady shear flow, e.g., elastic initially spherical particles[39–41] and capsule[42]. Numerical analyses of semi-dilute and jammed particle suspensions under oscillatory shear flow have been reported recently, e.g., rigid spherical particles at finite inertia[43], soft particle glasses[44], viscoelastic particles[45], bubbles[46], vesicles[47], and spherical capsule in dilute condition[48]. The recent theoretical work by Armstrong et al.[49] compared viscoelastic moduli obtained with several viscoelastic(-thixotropic) models and laboratory measurements under oscillatory shear flow. Matsunaga and Imai[48] systematically investigated the effect of viscosity ratio on the viscoelastic character of capsule suspension for a wide range of oscillatory shear rate frequencies. By employing continuum modeling, in particular the Oldroyd 8-constant framework, Saengow et al.[50] assessed the non-Newtonian character of human blood under uni-directional large-amplitude oscillatory shear (LAOS) flow, which is generated by superposing LAOS onto a steady shear flow. Clarifying the cellular-scale dynamics under oscillatory flow allows us to build precise continuum models of suspensions[51–53], and may lead us to novel biomedical applications[54], such as phenotype cell screening, and circulating tumor cell isolation in a chip[55]. However, this can be achieved only after fully grasping the effect of the particle deformations induced by the oscillations of the bulk suspension.

Therefore, the objective of this study is to clarify the relationship between the behavior of individual RBCs especially under SAOS flows and the viscoelastic character of dense suspension of RBCs. The contribution of the individual deformed RBC to the bulk suspension rheology is quantified by the stresslet tensor[56]. Here, the RBC is modeled as a biconcave capsule, whose membrane follows the Skalak constitutive law[57]. The internal and external fluid of the RBCs are modeled as Newtonian fluids and solved by the lattice-Boltzmann method (LBM), while the membrane mechanics with a finite-element method. The fluid and structure are fully coupled by an immersed boundary method[58]. We resort to graphics processing unit (GPU) computing to speed-up the above-mentioned numerical procedure. The same tools have been successfully applied to the analysis of the bulk suspension rheology of RBCs under steady shear flow in Takeishi et al.[11].

II. PROBLEM STATEMENTS

A. Flow and cell models

We consider a cellular flow consisting of plasma and RBCs with radius a_0 in a rectangular box of size $16a_0 \times 10a_0 \times 16a_0$ along the span-wise x, wall-normal y, and stream-wise z directions, with a resolution of 16 fluid lattices per radius
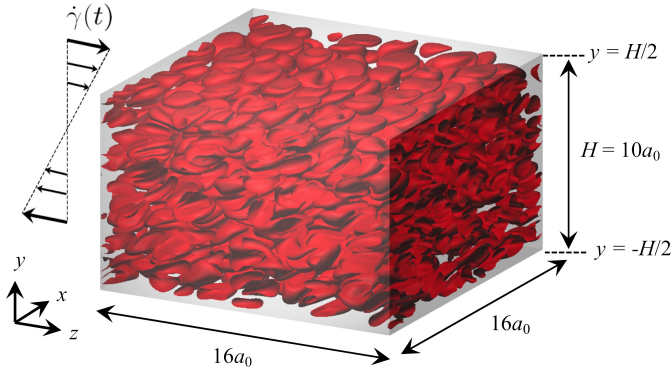
FIG. 1. Computational domain: a rectangular box of size $16a_0 \times 10a_0 \times 16a_0$ along the span-wise x, wall-normal y, and stream-wise z directions. Periodic boundary conditions are imposed on the two homogeneous directions (x and z directions). The oscillatory shear flow is generated by moving the top and bottom walls located at $y = \pm H/2$, where H (= $10a_0$) is the domain height. The snapshot depicts a dense suspension of RBCs ($\phi = 0.41$) with viscosity ratio $\lambda = 5$ and capillary number $Ca_0 = 0.05$.

of RBC. The size of the domain and the numerical resolution have been justified in our previous works[11,59]. Here, we further verified the effect of the wall-to-wall distance H as well as the cell-depleted peripheral layer (CDPL), see table I and Fig. 12 in appendix §A. Periodic boundary conditions are imposed on the two homogeneous directions (x and z directions). Each RBC is modeled as a biconcave capsule, i.e., a Newtonian fluid enclosed by a thin elastic membrane, with a major diameter of 8 μm (= $2a_0$), and maximum thickness of 2 μm (= $a_0/2$). The initial shape of the RBC is set to be the classical biconcave shape. A sketch of the computational domain, with the coordinate system used, is shown in Fig. 1 with an instantaneous visualisation of one of the dense cases, volume fraction $\phi = 0.41$ (the so-called discharge hematocrit, Hct_D).

The oscillatory shear flow is generated by moving the top and bottom walls located at $y = \pm H/2$ with velocity $U_{wall} = \pm \dot{\gamma}(t)H/2$, where H (= $10a_0$) is the domain height and $\dot{\gamma}(t)$ the shear rate, defined as

$$\dot{\gamma}(t) = \dot{\gamma}_0 \exp(i2\pi ft). \tag{1}$$

Here, $\dot{\gamma}_0$ is the shear-rate amplitude and f its frequency. The oscillatory strain $\gamma(t)$ is therefore defined as

$$\gamma(t) = \int \dot{\gamma}(t)dt = \frac{\dot{\gamma}_0}{i2\pi f}\exp(i2\pi ft) = \gamma_0 \exp(i2\pi ft - \pi/2), \tag{2}$$

where $\gamma_0 (= \dot{\gamma}_0/(2\pi f))$ is the strain amplitude. For the following analysis, we define the non-dimensional input frequency as $f_{in} = f/\dot{\gamma}_0$.

The membrane is modeled as an isotropic and hyperelastic material. The surface deformation gradient tensor $\mathbf{F}_s$ is given by

$$d\boldsymbol{x}_m = \mathbf{F}_s \cdot d\boldsymbol{X}_m, \tag{3}$$

where $\boldsymbol{X}_m$ and $\boldsymbol{x}_m$ are the membrane material points of the reference and deformed states, respectively. The local de-

formation of the membrane can be measured by the Green–Lagrange strain tensor

$$\mathbf{E} = \frac{1}{2}(\mathbf{C} - \mathbf{I}_s), \tag{4}$$

where $\mathbf{I}_s$ is the tangential projection operator. The two invariants of the in-plane strain tensor $\mathbf{E}$ can be given by

$$I_1 = \lambda_1^2 + \lambda_2^2 - 2, \quad I_2 = \lambda_1^2 \lambda_2^2 - 1 = J_s^2 - 1, \tag{5}$$

where λ_1 and λ_2 are the principal extension ratios. The Jacobian $J_s = \lambda_1 \lambda_2$ indicates the ratio of the deformed to the reference surface areas. The elastic stresses in an infinitely thin membrane are replaced by elastic tensions. The Cauchy tension $\mathbf{T}$ can be related to an elastic strain energy per unit area, $w_s(I_1, I_2)$:

$$\mathbf{T} = \frac{1}{J_s}\mathbf{F}_s \cdot \frac{\partial w_s(I_1, I_2)}{\partial \mathbf{E}} \cdot \mathbf{F}_s^T, \tag{6}$$

where the strain energy function w_s satisfies the Skalak (SK) constitutive law[57]

$$\frac{w_s}{G_s} = \frac{1}{4}\left(I_1^2 + 2I_1 - 2I_2 + CI_2^2\right). \tag{7}$$

In the expression above, G_s is the surface shear elastic modulus, and C a coefficient representing the area incompressibility. Substituting equation (7) into equation (6), we obtain the principal tensions in the membrane T_1 and T_2 with $T_1 \geq T_2$:

$$\frac{T_i}{G_s} = \frac{\lambda_i}{\lambda_j}\left[\lambda_i^2 - 1 + C\left(\lambda_i^2 \lambda_j^2 - 1\right)\right], \quad \text{for } (i,j) = (1,2) \text{ or } (2,1). \tag{8}$$

In this study, we set $C = 10^{260}$. Bending resistance is also considered[61], with a bending modulus $k_b = 5.0 \times 10^{-19}$ J[62]; these values have been shown to successfully reproduce the deformation of RBCs in shear flow and the thickness of the CDPL[59]. Note that the nodal forces on discrete elements, produced by bending energy, preserve the force- and torque-free principle. The reader is referred to Pozrikidis[63] for a precise description of bending resistance.

The internal (cytoplasm) and external (plasma) fluids are treated as Newtonian viscous fluids, which obey the incompressible Navier–Stokes equations. Although the large standard deviation of the values of the geometric and mechanical properties of healthy RBCs were presented depending on the use of different techniques, cytoplasmic viscosity of RBCs was summarized as 6.07 ± 3.8 mPa·s in Tomaiuolo[64]. The normal plasma viscosity, on the other hand, is $\mu_0 = 1.1$–1.3 cP (1.1–1.3 mPa·s) at 37 °C[65]. Hence, physiologically relevant values of the viscosity ratio lie in the range λ (= μ_1/μ_0) = 1.89–8.23 if the plasma viscosity is set to be $\mu_0 = 1.2$ cP. The viscosity ratio $\lambda = 5$ is adopted for most of the results presented in this study, except when specifically investigating the role of λ on the suspension rheology. In this case, the range $\lambda = 0.1$–10 is investigated.

In the inertialess limit, the problem is characterised by the capillary number,

$$Ca_0 = \frac{\mu_0 \dot{\gamma}_0 a_0}{G_s}, \tag{9}$$

in addition to the non-dimensional input frequency $f_{in} = f/\dot{\gamma}_0$ and the viscosity ratio λ introduced above. The capillary number quantifies the relative importance of elastic and viscous forces, with highly deformable cells characterised by large values of Ca_0. To limit the computational cost and yet obtain results not affected by inertial effects, we set the Reynolds number $Re = \rho \dot{\gamma}_0 a_0^2/\mu_0 = 0.2$, where ρ is the plasma density. This value well reproduces the capsule dynamics in unbounded shear flows obtained with the boundary integral method in Stokes flow (see also Figures 12 and 13 in Takeishi et al. [11]). We further investigate the effect of Re on the Stokes boundary layer in appendix §B and confirmed that the layer remained the same even at lower $Re(= 0.05)$ as shown in Fig. 13.

B. Numerical method

The finite-element method (FEM) is used to solve the weak form of the equations governing the inertialess membrane dynamics and obtain the load q acting on the membrane:

$$\int_S \hat{u}\cdot q\, dS = \int_S \hat{\varepsilon} : \mathbf{T}\, dS, \tag{10}$$

where $\hat{u}$ and $\hat{\varepsilon} = (\nabla_s \hat{u} + \nabla_s \hat{u}^T)/2$ are the virtual displacement and virtual strain, respectively. The in-plane elastic tension $\mathbf{T}$ is obtained from the Skalak constitutive law, see equation (7).

The Navier–Stokes equations for the internal and external fluids are discretised by the LBM based on the D3Q19 model[66,67]. In the LBM, the macroscopic flow is obtained by collision and streaming of hypothetical particles described by the lattice-Boltzmann-Gross-Krook (LBGK) equation[68], which is given as

$$f_i\left(x_f + c_i\Delta t, t + \Delta t\right) - f\left(x_f, t\right)$$
$$= -\frac{1}{\tau}\left[f_i\left(x_f, t\right) - f_i^{eq}\left(x_f, t\right)\right] + F_i\Delta t, \tag{11}$$

where f_i is the particle distribution function for particles with velocity c_i ($i = 0$–18) at the fluid node x_f, Δt is the time step size, f_i^{eq} is the equilibrium distribution function, τ is the non-dimensional relaxation time, and F_i is the external force applied from the membrane material points, obtained with the immersed boundary method (IBM)[58]. The membrane force at the membrane node x_m is distributed to the neighboring fluid nodes x_f using a smoothed delta function approximating the Dirac delta function as

$$D(x) = \begin{cases} \dfrac{1}{64\left(\Delta x_f\right)^3}\prod_{k=1}^3\left(1 + \cos\dfrac{\pi x_k}{2\Delta x_f}\right) & \text{if } |x_k| \leq 2\Delta x_f, \\ 0 & \text{otherwise,} \end{cases} \tag{12}$$

where $k \in [1,3]$ and $x_1 = x$, $x_2 = y$, $x_3 = z$. Similarly, the velocity at the membrane node $v(x_m)$ is obtained by interpolating the velocities at the fluid nodes. The membrane node x_m is updated by Lagrangian tracking with the no-slip condition, i.e.

$$\frac{dx_m}{dt} = v(x_m). \tag{13}$$

The explicit fourth-order Runge–Kutta method is used for time-integration.

In our coupling of method of LBM and IBM, the hydrodynamic interaction between individual RBCs is solved without modeling a non-hydrodynamic inter-membrane repulsive force in the case of vanishing inertia, as also shown in Figure 13 in Takeishi et al. [11]. The volume-of-fluid (VOF) method[69] and front-tracking method[70] are employed to update the viscosity in the fluid lattices. A volume constraint is implemented to counteract the accumulation of small errors, leading to changes in the volume of the individual cells[71]: in our simulation, the volume error is always maintained lower than 10^{-3}%. All numerical procedures are fully implemented on GPU to accelerate the numerical simulation. For further details of the methods we refer to our previous works[11,72]. The mesh size of the LBM for the fluid solution is set to be 250 nm, and that of the finite elements describing the membrane is also approximately 250 nm (an unstructured mesh with 5,120 elements is used for each cell). This resolution has been shown to successfully represent single- and multi-cellular dynamics[59]; we have verified that the results of multi-cellular dynamics are not changing with twice the resolution for both the fluid and membrane[59]. We have further investigated the distance between neighboring membrane nodes. The result of time-averaged distance of neighboring membrane nodes $\langle\Delta_{\text{node}}\rangle$ for different volume fractions ϕ is discussed in appendix §C.

C. Analysis of capsule suspensions

For the following analysis, the behavior of RBCs subjected to oscillatory shear flow is quantified by the length of the semi-major axis a_{max} and orientation angle θ between the major axis of the deformed RBC and the shear direction. The length of the semi-major axis a_{max} of the deformed RBC is obtained from the eigenvalues of the inertia tensor of an equivalent ellipsoid approximating the deformed RBC[73]. The orientation angle θ of a single deformable spherical capsule converges to $\pi/4$ in shear flow as $Ca \to 0$[35,74].

The suspension rheology of RBCs, or the contribution of the suspended RBCs to the bulk viscosity, is quantified by the particle stress $\Sigma^{(p)}$[56]. Specifically, for a deformable capsule and any viscosity ratio, Pozrikidis[75] analytically derived an expression for the corresponding stresslet, so that the particle contribution to the total stress can be written as:

$$\Sigma^{(p)} = \frac{1}{V}\sum_{i=1}^N \mathbf{S}_i, \tag{14}$$

$$= \frac{1}{V}\sum_{i=1}^N \int_{A_i}\left[\frac{1}{2}\left(r\hat{q} + \hat{q}r\right) - \mu_0\left(1 - \lambda\right)\left(vn + nv\right)\right]dA_i, \tag{15}$$

where V is the volume of the domain, $\mathbf{S}_i$ the stresslet of the i-th RBC (or capsule), $\mathbf{r}$ is the membrane position relative to the centre of the RBC, $\hat{q}$ the load acting on the membrane including the contribution from the bending rigidity, μ_0 the outer fluid (plasma) viscosity, v the interfacial velocity of the membrane, and A_i the membrane surface area of the i-th RBC. Here, the suspension shear viscosity $\mu_{all}(= \mu_0 + \delta\mu)$ is represented by the viscosity μ_0 of the carrier fluid (plasma) and a perturbation $\delta\mu$. This leads to the introduction of the relative viscosity μ_{re} and of the specific viscosity μ_{sp} defined as:

$$\mu_{re} = \frac{\mu_{all}}{\mu_0} = 1 + \mu_{sp}, \tag{16}$$

$$\mu_{sp} = \frac{\delta\mu}{\mu_0} = \frac{\Sigma_{12}^{(p)}}{\mu_0\dot{\gamma}_0}, \tag{17}$$

where the subscript $_1$ represents the streamwise direction (i.e., the z-direction in this study) and the subscript $_2$ the wall-normal direction (i.e., the y-direction in this study). Using the diagonal components of the particle stress $\Sigma_{ii}^{(p)}$, the first and second normal stress differences, typically used to quantify the suspension viscoelastic behavior, can be defined as:

$$\frac{N_1}{\mu_0\dot{\gamma}_0} = \frac{\Sigma_{11}^{(p)} - \Sigma_{22}^{(p)}}{\mu_0\dot{\gamma}_0}, \tag{18}$$

$$\frac{N_2}{\mu_0\dot{\gamma}_0} = \frac{\Sigma_{22}^{(p)} - \Sigma_{33}^{(p)}}{\mu_0\dot{\gamma}_0}. \tag{19}$$

In the case of small oscillations, the particle stress $\Sigma_{12}^{(p)}(t)$ is also an oscillatory function, defined by the amplitude $|\Sigma_{12}^{(p)}|^{amp}$ and the phase difference δ ($-\pi/2 \leq \delta \leq 0$) between $\Sigma_{12}^{(p)}(t)$ and the input shear rate $\dot{\gamma}(t)$:

$$\Sigma_{12}^{(p)}(t) = |\Sigma_{12}^{(p)}|^{amp} \exp\{i(2\pi\mathrm{f}t + \delta)\}. \tag{20}$$

Following classical rheological analyses, the frequency-dependent rheology of particle suspensions is expressed in terms of a complex modulus G^* and a complex viscosity η^*. Using the fluid strain $\gamma(t)$, G^* is given by:

$$G^* = \frac{\Sigma_{12}^{(p)}(t)}{\gamma(t)} = \frac{i|\Sigma_{12}^{(p)}|^{amp}}{\gamma_0} \exp(i\delta) = G' + iG'', \tag{21}$$

where G' is the storage modulus and G'' is the loss modulus defined as:

$$\begin{cases} G' = -\dfrac{2\pi\mathrm{f}|\Sigma_{12}^{(p)}|^{amp}}{\dot{\gamma}_0}\sin\delta, \\[3mm] G'' = \dfrac{2\pi\mathrm{f}|\Sigma_{12}^{(p)}|^{amp}}{\dot{\gamma}_0}\cos\delta. \end{cases} \tag{22}$$

Using the applied shear $\dot{\gamma}(t)$, instead, one can introduce a complex viscosity η^*, given by:

$$\eta^* = \frac{\Sigma_{12}^{(p)}(t)}{\dot{\gamma}(t)} = \frac{|\Sigma_{12}^{(p)}|^{amp}}{\dot{\gamma}_0} \exp(i\delta) = \eta' - i\eta'', \tag{23}$$

where η' and η'' are the viscous and elastic component of η^*, respectively[76], and are defined as:

$$\begin{cases} \eta' = \dfrac{|\Sigma_{12}^{(p)}|^{amp}}{\dot{\gamma}_0}\cos\delta = \dfrac{G''}{2\pi\mathrm{f}}, \\[3mm] \eta'' = -\dfrac{|\Sigma_{12}^{(p)}|^{amp}}{\dot{\gamma}_0}\sin\delta = \dfrac{G'}{2\pi\mathrm{f}}. \end{cases} \tag{24}$$

In the following analysis, η' and η'' are normalized by μ_0, and hence, the moduli are rewritten as:

$$\begin{cases} \dfrac{\eta'}{\mu_0} = |\mu_{sp}|^{amp}\cos\delta, \\[3mm] \dfrac{\eta''}{\mu_0} = -|\mu_{sp}|^{amp}\sin\delta, \end{cases} \tag{25}$$

where $|\mu_{sp}|^{amp}(= |\Sigma_{12}^{(p)}|^{amp}/(\mu_0\dot{\gamma}_0))$ is the magnitude of the specific viscosity.

The oscillations are examined after the fully-developed regime has been reached. At least after non-dimensional time $\dot{\gamma}_0 t \geq 40$, the influence of the initial conditions on the specific viscosity was negligible[11]. In this study, therefore, the oscillations will be applied after this time, which is redefined as $\dot{\gamma}_0 t = 0$ for simplicity. The dominant frequency for the input $\dot{\gamma}(t)$ and output $\mu_{sp}(t)$ are obtained with a discrete Fourier transform (DFT), using the *Fastest Fourier Transform in the West* (*FFTW*) library[77]. The frequency peak of the output signal corresponds to the frequency of the applied shear for all cases considered here. The details of the DFT analysis adopted in this study are reported in the appendix §D. To reduce the influence of the initial conditions, the DFT analysis and the spatial-temporal average denoted as $\langle\cdot\rangle$ start once the amplitude of μ_{sp} becomes basically constant; as an example, for $f_{in} = 0.1$, the analyses start from the non-dimensional time $\dot{\gamma}_0 t = 800$, and continues for 12 periods (see Fig. 2c). For all the cases, one output wave is resolved by at least 100 discrete times, and over 10 wave periods are considered in the DFT analysis. The effect of the number of periods on the calculated values are discussed in the appendix §E. When presenting the results, we will initially focus on the analysis of suspensions in physiological conditions, with volume fraction $\phi = 0.41$, $\lambda = 5$, and $Ca_0 = 0.05$, and later consider variations of the viscosity ratio λ, volume fraction ϕ and capillary number Ca_0.

III. RESULTS

A. Dense suspension of RBCs under oscillatory flow

First, we investigate the oscillatory behavior of dense suspension of RBCs under SAOS flow at $Ca_0 = 0.05$. A snapshot of the numerical results for the lowest input shear frequency investigated in this study $f_{in} = 0.01$ is shown in Fig. 2(a), while the time history of the specific viscosity $\mu_{sp}(t)$ and shear-rate $\dot{\gamma}(t)$ are displayed in Fig. 2(b), where the value of μ_{sp} obtained under steady shear flow is also displayed with dashed line for comparison. As expected, the magnitude of μ_{sp} at the lowest shear frequency f_{in} is similar to that obtained under steady

shear flow, and the output wave, μ_{sp}, responds to the imposed shear, $\dot{\gamma}$, without significant delay. When the shear frequency f_{in} increases, the resultant amplitude $|\mu_{sp}|^{amp}$ is reduced, as shown in Figs. 2(c) and 2(d). Furthermore, there is a clear phase delay between the μ_{sp} and $\dot{\gamma}$ oscillations, with the phase difference increasing as f_{in} increases. The rate of decrease in the amplitude of the specific viscosity $|\mu_{sp}|^{amp}$ shown in Fig. 2(c) is only 0.00781 over a non-dimensional time of $\dot{\gamma}_0 t = 100$, starting from $\dot{\gamma}_0 t = 800$. Thus, the results that we discuss later, e.g., in Fig. 4 can be considered to be fully converged.

We display the time history of the orientation angle θ, of the specific viscosity μ_{sp} and of the normal stress difference N_i (with $i = 1, 2$) in Fig. 3; the instantaneous values are averaged over the different RBCs, normalized by their amplitude χ_{amp}, and shifted by their mean value χ_m. The period is also normalized by the inverse frequency $1/f_{in}$ of each case. The plots show that θ is slightly delayed from the imposed shear (Fig. 3a), and this delay becomes greater for larger frequencies. Thus, the time signal of the oscillatory rheology μ_{sp} adapts to the change in the imposed shear faster than the RBCs orientation θ. Despite this delay, θ has the same period as μ_{sp}, independently of the applied frequency. The normal stress differences N_i, on the other hand, exhibit a period which is almost half that of the imposed shear (μ_{sp} and θ), and it increases with the oscillation frequency. The first normal stress difference N_1 tends to synchronise with the imposed shear (μ_{sp} and θ), while the second normal stress difference N_2 is basically in opposite phase. These results remain the same in dilute conditions ($\phi = 0.11$).

The frequency-dependent deformation and orientation of individual RBCs are investigated to understand their link to the flow rheology. The deformation is characterised by the maximal radius a_{max}, with the ratio a_{max}/a_0 chosen as a deformation index. The spatial-temporal averages of these two observables are shown in Figs. 4(a) and 4(b) versus the oscillation frequency f_{in}. The value of $\langle a_{max}\rangle/a_0$ is slightly non-monotonic, first growing till $f_{in} \approx 1$ and then decreasing. Especially for the middle range of f_{in} ($0.05 \leq f_{in} \leq 1$), $\langle a_{max}\rangle/a_0$ is greater than in steady shear flow. However, the frequency-induced mean deformation differs by only 0.8% from that in steady shear flow even for the maximum $\langle a_{max}\rangle/a_0$ at $f_{in} = 0.5$ (Fig. 4a). The amplitude of the fluctuations around the mean keeps instead reducing as f_{in} grows. The orientation angles θ/π fluctuate around zero for all f_{in}, and thus, the values are lower than those obtained under steady shear flow, with no significant frequency dependence, as shown in Fig. 4(b).

The first and second normal stress differences $\langle N_i\rangle/\mu_0\dot{\gamma}_0$, the resultant amplitude $|\mu_{sp}|^{amp}$ and phase difference δ are shown in Figs. 4(c), 4(d) and 4(e) for the different frequencies under consideration. The magnitude of $|\langle N_i\rangle|/\mu_0\dot{\gamma}_0$ decreases monotonically from that in the steady shear flow as f_{in} increases, reaching nearly zero for the highest value of f_{in}. The first normal stress difference $\langle N_1\rangle$ is positive, while $\langle N_2\rangle$ is negative (Fig. 4c). It is known that the ratio $N_2/N_1 = -0.5$ can be typically observed in liquid crystals consisting of rod-like polymer solutions[78]. Although our numerical results do no follow this, the order of magnitude of the ratio is $O(-\langle N_2\rangle/\langle N_1\rangle) \approx 10^{-1}$, and almost independent of ϕ. The

error bars for $\langle N_i\rangle/\mu_0\dot{\gamma}_0$ are displayed only on one side of the mean value for major clarity. The specific viscosity $|\mu_{sp}|^{amp}$ also decreases from the value in steady shear flow as f_{in} increases above the lowest value (Fig. 4d). The specific viscosity $|\mu_{sp}|^{amp}$ only weakly changes in the intermediate range of f_{in} ($0.05 \leq f_{in} \leq 0.5$), before decreasing again at higher f_{in}. The phase delay δ is also found to be a function of the shear frequency, as documented in Fig. 4(e), where we observe that δ decreases from almost zero at the lowest f_{in} (= 0.01) until $f_{in} = 1$, and then increases for $f_{in} > 1$.

The frequency-dependent $|\mu_{sp}|^{amp}$ and δ define the complex viscosity, with real and imaginary part η' and η'', which are reported in Fig. 4(f). The variations of η' with f_{in} well follow $|\mu_{sp}|^{amp}$, whereas η'' first increases, reaches a maximum at $f_{in} \approx 1$, and then decreases again for larger frequencies. While η'' almost coincides with η' at large f_{in}, the increase of η'' at low f_{in} can be well approximated by a power law: $\eta'' \propto f_{in}^{0.47}$. This result indicate that dense suspensions of RBCs cannot be fully modelled as Maxwell fluids, where the complex shear moduli $\eta''(= G'/(2\pi f)) \approx f$ and $\eta'(= G''/(2\pi f)) \approx const$ for low f; on the other hand, the results of η'' are qualitatively similar to those obtained with the Oldroyd-B fluids[78,79]. However, since an Oldroyd-B fluid is characterised by zero N_2[78,79], RBCs (or SK capsule) suspension differ from the aforementioned non-Newtonian models.

At the microstructure level, the RBCs fully orient towards the shear directions at the low frequency ($f_{in} = 0.05$) except for the lowest one ($f_{in} = 0.01$), while their orientations vary for high frequencies ($f_{in} \geq 0.1$) because individual RBCs are forced to reorient before reaching a stable condition. Consequently, the standard deviations of the orientation angle θ are greater at low frequency and smaller at high frequencies (Fig. 4b). The results are consistent with those described later in Figs. 6(b), 9(d) and 9(e). Although it is known that the RBC deformation alone is sufficient to give rise to shear-thinning[42], the resulting complex viscosity shown in the Fig. 4(f) weakly depends on the frequency-modulated deformations or orientations of individual RBCs (Figs. 4a and 4b, respectively), but rather depends on combinations of the frequency-dependent amplitude $|\mu_{sp}|^{amp}$ and phase difference δ (Figs. 4d and 4e, respectively).

To conclude, we present the Lissajous-Bowditch plots[80,81] of μ_{sp} versus $\dot{\gamma}/\dot{\gamma}_0$, following the classical way to analyse nonlinear oscillations. We recall that an elastic solid would correspond to a straight line, a Newtonian fluid to a perfect circle, and viscoelastic materials under SAOS to an ellipsoid. Nonlinear responses can generally lead to a more complex shape, which itself is a characterization of the nonlinear viscoelasticity of the suspension[80], as usually observed under LAOS. The diagrams for our RBC suspensions are shown in Fig. 5, where the Lissajous plots reveal deviation from the ellipsoidal to the sigmoidal shape as f_{in} decreases.

B.   Effect of the viscosity ratio

Next, we investigate the effect of the viscosity ratio λ (= 0.1, 1, 5 and 10) on the system viscoelasticity for relatively
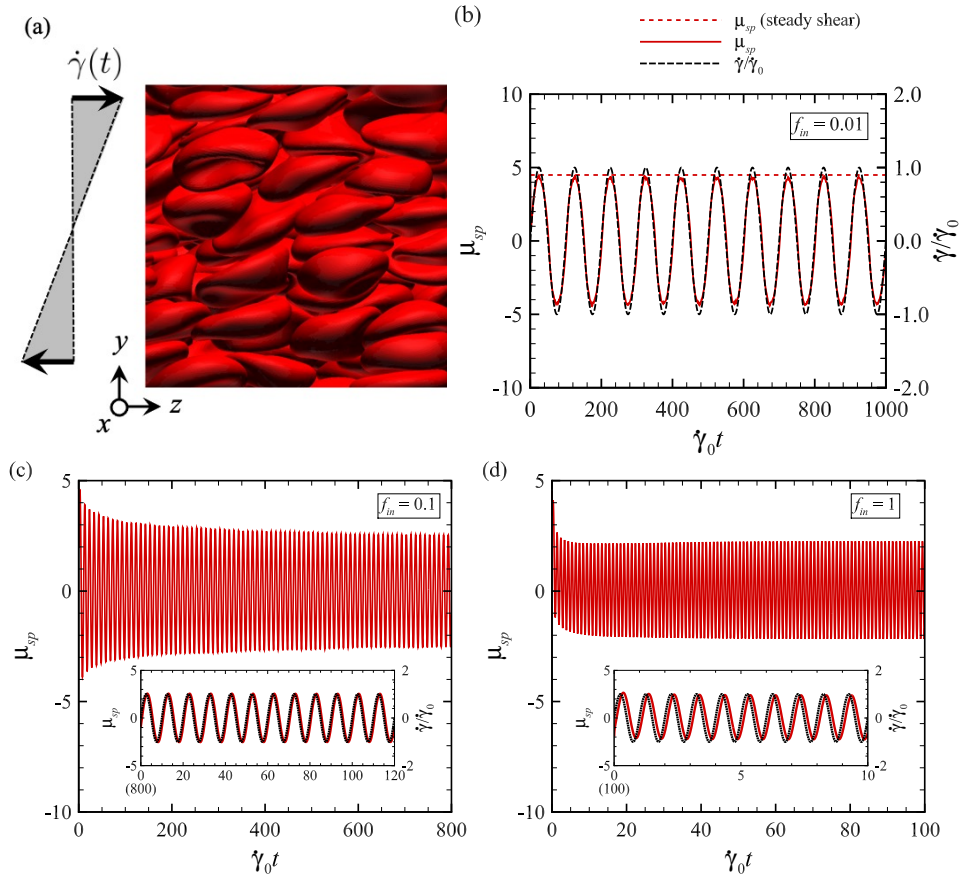
FIG. 2. (a) Snapshot of a dense suspension of RBCs ($\phi = 0.41$) zooming on the central part of the rectangular computational box for the lowest shear frequency $f_{in} = 0.01$ under consideration. (b) Time history of the specific viscosity μ_{sp} and input shear rate $\dot{\gamma}/\dot{\gamma}_0$ under $f_{in} = 0.01$, where $\dot{\gamma}$ is normalized by the amplitude $\dot{\gamma}_0$. The result of μ_{sp} obtained under steady shear flow is also displayed as red dashed line. (c and d) Time history of μ_{sp} and $\dot{\gamma}$ for shear frequencies $f_{in} =$ (c) 0.1 and (d) 1. The results are obtained with $\phi = 0.41$, $\lambda = 5$, and $Ca_0 = 0.05$.

low and high frequencies f_{in} (= 0.05 and 0.5). The behavior of $\langle a_{max} \rangle / a_0$ and $\langle \theta \rangle / \pi$ as a function of λ is reported in Figs. 6(a) and 6(b). The mean deformation of individual RBCs progressively increases with λ, with only a slight increase at low f_{in} (= 0.05), and a more significant one for f_{in}= 0.5, when comparing with the case of steady shear flow (Fig. 6a).

The average cell orientation $\langle \theta \rangle / \pi$ decreases under oscillatory shear flow, with no significant differences in the mean values for the different λ considered (Fig. 6b). When the shear frequency is small ($f_{in} = 0.05$), the RBCs are able to attain a similar orientation (i.e., small standard deviations of $\langle \theta \rangle / \pi$), while when the shear frequency is large ($f_{in} = 0.5$), the ordered orientation is disrupted, as shown by the large value of standard deviations in Fig. 6(b). This is consistent with the observations from the data for $\lambda = 5$ discussed above, cf. Fig. 4(b).

As also noted before from the data in Figs. 4(c) and 4(d), $|\langle N_i \rangle|/\mu_0 \dot{\gamma}_0$ and $|\mu_{sp}|^{amp}$ decrease under oscillatory shear flow, and this behavior is consistently observed also for the different values of λ under consideration (Figs. 6c and 6d). $\langle N_1 \rangle$ only slightly increases with λ at low f_{in}, while it exhibits an opposite tendency at high f_{in}; furthermore, there are no sig-

nificant variations in $\langle N_2 \rangle$ between high and low f_{in}. In particular, $|\mu_{sp}|^{amp}$ increases with λ, similarly to what observed for steady shear flow. For low viscosity ratios, $|\mu_{sp}|^{amp}$ progressively reduces with f_{in}, while for large viscosity ratios, it does not vary significantly with the frequency of the imposed shear f_{in}. The phase difference $\langle \delta \rangle / \pi$ instead does not vary significantly with the viscosity ratio for small values of f_{in}, while it does change significantly (i.e., the magnitude of δ decreases as λ increases) for the largest value of f_{in} (see Fig. 6e). In other words, large values of the viscosity ratios help to reduce the time-lag between the input and output signal at high shear frequency as compared to steady shear.

The complex viscosity is displayed in Fig. 6(f) as a function of λ for the two values of f_{in} under investigation. For all the values of the viscosity ratio, η' well follows $|\mu_{sp}|^{amp}$, while η'' is only weakly dependent on λ. At the large f_{in} (= 0.5), η' overcomes η'' between $\lambda = 1$ and 5, while such crossover is not found at low f_{in} (= 0.05). The viscous component η' is higher at the low f_{in} than at the large one, while η'' follows an opposite trend, i.e., its value is higher at the large f_{in} than at the low frequencies.

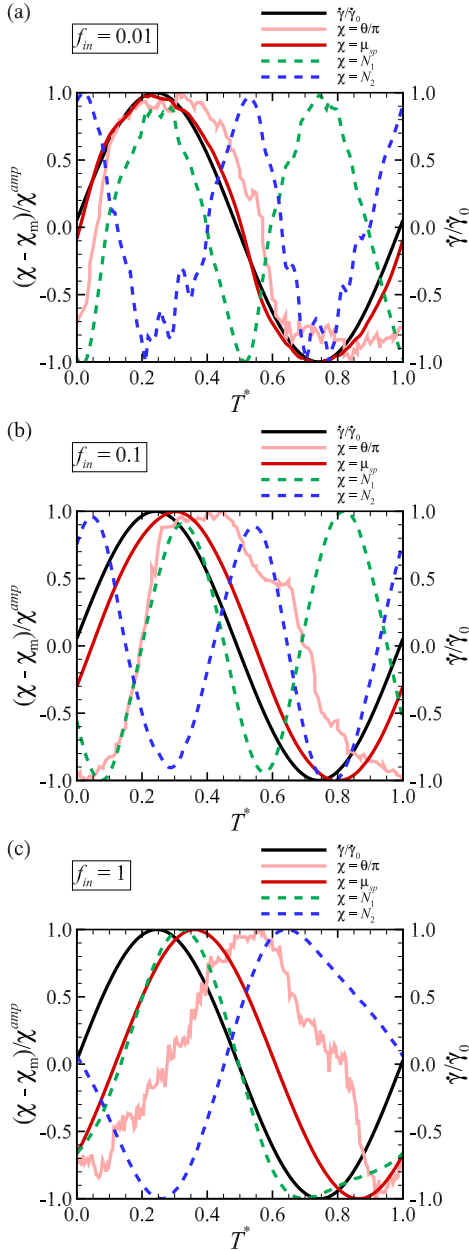Overall, the rheological behavior of the RBC suspension in oscillating shear flows appears to be only weakly dependent

FIG. 3. Time history of the orientation angle θ and rheological parameters [the specific viscosity μ_{sp} and the normal stress differences N_i ($i = 1, 2$)], during a specific period T^* at statistical steady state after the initial transient, for different frequencies $f_{in} = $ (a) 0.01, (b) 0.1 and (c) 1, where the period is normalized by the inverse frequency $1/f_{in}$. The values are averaged between individual RBCs, normalized by each amplitude χ_{amp} and shifted so that each baseline is the mean value χ_m. The results are obtained with $\phi = 0.41$, $\lambda = 5$, and $Ca_0 = 0.05$.

of the viscosity ratio, except for the lower phase lag observed at high λ.

C.   Effect of the volume fraction

We performed simulations in a dilute condition ($\phi = 0.11$) to investigate the behavior at low volume fractions, characterised by fewer cell-cell interactions. The results for different oscillation frequencies at $\phi = 0.11$ are compared to those at $\phi = 0.41$ in Fig. 7, following the same order as in Figs. 4 and 6.

In dilute conditions, the deformation index, $\langle a_{max} \rangle / a_0$, remains almost the same as in dense conditions, but with smaller fluctuations than at larger volume fractions, as indicated by the error bar (Fig. 7a). Although frequency-induced deformations are found in the intermediate range of f_{in} ($0.0333 \leq f_{in} \leq 1$), all the variations with respect to the case of steady shear flow are always less than 1%. The mean orientation $\langle \theta \rangle / \pi$ and its fluctuations also remain similar to those in the dense suspension, as shown in Fig. 7(b), with $\langle \theta \rangle / \pi$ fluctuating around zero for all f_{in}, resulting in a lower average $\langle \theta \rangle / \pi$ than under steady shear flow.

The spatio-temporal average of the first and second normal stress differences $\langle N_i \rangle$, the specific viscosity $|\mu_{sp}|^{amp}$ and of the phase shift δ are shown as a function of f_{in} in Figs. 7(c), 7(d) and 7(e). As for the flow of dense suspensions, $\langle N_i \rangle / \mu_0 \dot{\gamma}_0$ and $|\mu_{sp}|^{amp}$ decrease from the steady-shear flow value as f_{in} increases. The values of $\langle N_i \rangle$ decrease by one order of magnitude from $\phi = 0.41$ to $\phi = 0.11$. The specific viscosity $|\mu_{sp}|^{amp}$ basically decreases with f_{in}. The trend is similar to that observed in dense conditions, although $|\mu_{sp}|^{amp}$ is clearly lower at low volume fraction. For both volume fractions under investigation, a first plateau with lower $|\mu_{sp}|^{amp}$ amplitude occurs at $f_{in} \approx 0.05$ before the final decay for high frequencies.

The behavior of δ / π in dilute conditions, on the other hand, is different from that in the dense suspension: in this case, δ / π monotonically decreases as f_{in} increases, see panel (e) of Fig. 7. Because of this, at relatively high forcing frequencies, $f_{in} \geq 1$, the magnitude of δ / π becomes greater in the dilute condition than in the dense case (cf. Fig. 7e).

Figure 7(f) reports the complex viscosity. The real part, η', again well follows the trend discussed for $|\mu_{sp}|^{amp}$, whereas η'' attains its maximum value around $f_{in} = 0.5$ and then crosses over η' for larger frequencies. At low frequencies, we estimate η'' to increase with f_{in} following a power law with exponent 0.53, i.e., $\eta'' \propto f_{in}^{0.53}$.

Overall, the volume fraction clearly affects the mean specific viscosity μ_{sp} in SAOS flows; however the differences due to volume fraction reduce at higher oscillations frequencies. The other observables appear instead to be almost independent of the volume fraction. High frequency or dilute conditions decrease the rate of hydrodynamic interaction between RBCs, resulting in a reduced contribution of the RBCs to the suspension bulk properties, as observed for the normal stress differences $\langle N_i \rangle$.

A frequency sweep data typically reveals the characteristic microstructural relaxation time scales in the system, often identified as the intersection of the two complex moduli. In our case, η' and η'' show change in behavior for $f_{in} \geq 1$ for both $\phi = 0.11$ and 0.41, (Fig. 7f). Also, the normal stress differences $\langle N_i \rangle$ vanish above this value of f_{in}, and δ changes behavior (Fig. 7e). Intriguingly, this frequency corresponds
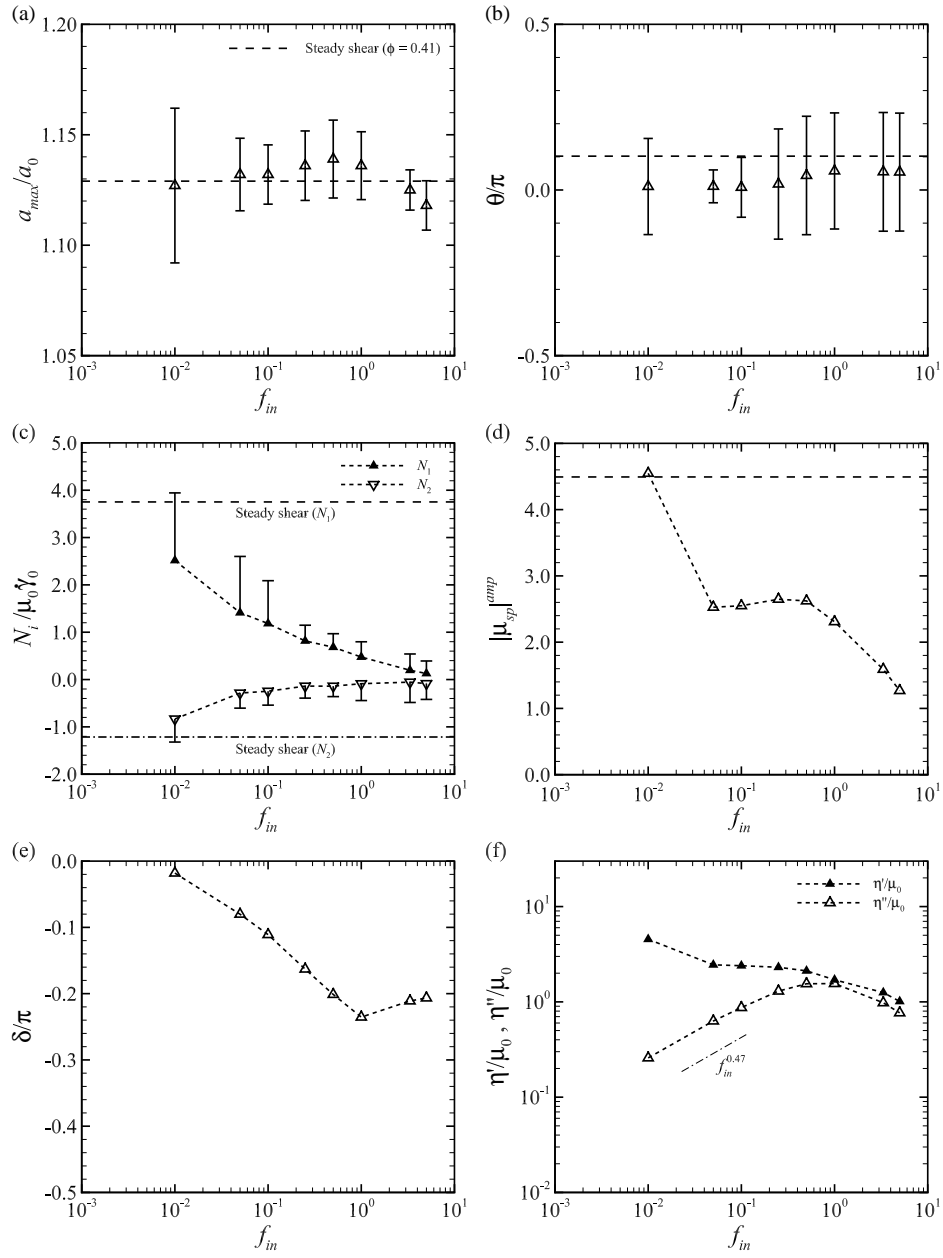
FIG. 4. (a) Spatial-temporal average of the deformation index $\langle a_{max}\rangle/a_0$, (b) orientation angle $\langle\theta\rangle/\pi$ between the major axis of the deformed RBC and the shear direction, (c) the first and second normal stress differences $\langle N_i\rangle/\mu_0\dot{\gamma}_0$ ($i = 1$ and 2), (d) amplitude of the specific viscosity μ_{sp}, (e) phase difference δ, and (f) complex viscosity η'/μ_0 and η''/μ_0 as a function of the input frequency f_{in}. The results obtained under steady shear flow are also displayed in (a)–(d) as dashed (or dash-dot) lines. The error bars in (a)–(c) represent standard deviations. The error bars in panel (c) are displayed only on one side of the mean value for major clarity. The results are obtained with $\phi = 0.41$, $\lambda = 5$ and $Ca_0 = 0.05$.

to the rotation time scale $\dot{\gamma}_0^{-1}$, which is equal to the tumbling time scale of rigid particles suspended in a simple shear flow.

D.   Effect of the capillary number

In this section, we consider the relatively large capillary number $Ca_0 = 0.8$, and quantify its effect on the complex viscosity for different values of the volume fraction ϕ (=

0.11–0.41). Even in such large Ca_0 condition, the Lissajous-Bowditch plots shown in Fig. 8 exhibit an elliptical shape, which is the characteristic response in SAOS, independently of the value of f_{in}. Snapshots of the suspension of RBCs subject to low and large capillary number, $Ca_0 = 0.05$ and 0.8, at $f_{in} = 0.5$ and for different volume fractions ϕ are shown in Fig. 9(a). Also, the spatio-temporal average of the deformation $\langle a_{max}\rangle/a_0$ and of the orientation angle $\langle\theta\rangle/\pi$ are shown in Figs. 9(b)–9(e) for both low Ca_0 (= 0.05) and high Ca_0 (=
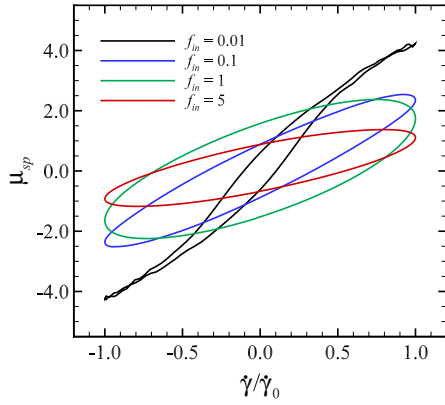
FIG. 5. Lissajous-Bowditch plots of μ_{sp} versus $\dot{\gamma}/\dot{\gamma}_0$ for different f_{in}. The results are obtained with $\phi = 0.41$, $\lambda = 5$ and $Ca_0 = 0.05$.

0.8).

Starting from Fig. 9(b), we note that the deformation $\langle a_{max}\rangle/a_0$ remains almost the same for low Ca_0 (= 0.05), independently of f_{in} (= 0.05 and 0.5) and ϕ; the values are close to those obtained for steady shear flow (see the black dashed line in the figure). On the other hand, for the large Ca_0 (= 0.8) condition, we observe a difference between the low and high f_{in}; in particular, $\langle a_{max}\rangle/a_0$ is larger at $f_{in} = 0.05$ than at $f_{in} = 0.5$, also with larger variations around the mean (see error bars in Fig. 9c). We therefore observe that the deformation is impeded by oscillatory flows. For the lowest value considered, $\phi = 0.11$, we do not observe relatively large variations of the average deformation at $f_{in} = 0.5$, suggesting that the decrease of deformation with frequency is due to hydrodynamic interactions among the different cells.

In the results presented so far, $\langle\theta\rangle/\pi$ is found to fluctuate around zero, resulting in a lower value of $\langle\theta\rangle/\pi$ than that for steady shear flow. This is observed also when f_{in}, ϕ, and Ca_0 change as shown in Figs. 9(d) and 9(e). The fluctuations of $\langle\theta\rangle/\pi$ are larger for high-frequency oscillatory shear, which is similar to the results for different viscosity ratios λ presented in Fig. 6(b). As mentioned above or in appendix §C, high frequency or dilute conditions decrease the rate of hydrodynamic interaction between RBCs, resulting in a reduced contribution of the RBCs to the suspension bulk properties. Thus, large fluctuations of $\langle\theta\rangle/\pi$ at high frequency come from various orientations of the individual RBCs due to weak hydrodynamic interactions, independently of ϕ and Ca_0.

The spatio-temporal average of the specific viscosity $|\mu_{sp}|^{amp}$ and of the phase delay δ/π are compared for low Ca_0 (= 0.05) and high Ca_0 (= 0.8) in panels (a)–(d) of Fig. 10. As expected, the specific viscosity increases with the RBC volume fraction: $|\mu_{sp}|^{amp}$ is maximum for steady shear flow and decreases under oscillatory shear flow. For the smallest Ca_0 (= 0.05), $|\mu_{sp}|^{amp}$ is almost independent of the frequency of the imposed shear f_{in}, at least for the range considered in this study, deemed relevant for physiological flows. For the large Ca_0 (= 0.8) flow, $|\mu_{sp}|^{amp}$ appears to decrease with f_{in}. For both low and high Ca_0, the frequency-dependent decrease of $|\mu_{sp}|^{amp}$ becomes more evident as ϕ increases. We can also

note in the figure that $|\mu_{sp}|^{amp}$ is lower for the largest value of the capillary number investigated at steady shear rate. As high Ca_0 corresponds to large deformability in the limit $f_{in} \to 0$, this result confirms the shear-thinning behavior with deformability in the case of suspensions of deformable objects[40,41,82].

As discussed when examining the results in Fig. 6(e), the magnitude of δ/π increases at high f_{in} for every volume fraction ϕ, independently of Ca_0 as shown in Figs. 10(c) and 10(d). Furthermore, the magnitude of δ/π also depends on ϕ: at low f_{in} (= 0.05), $|\delta|/\pi$ slightly increases as ϕ increases for low Ca_0 (Fig. 10c). On the other hand, at high f_{in} (= 0.5), $|\delta/\pi|$ decrease as ϕ increases, especially for large Ca_0 conditions. Overall, the phase difference $|\delta/\pi|$ is largest for the lowest ϕ (= 0.11), high f_{in} (= 0.5), and high Ca_0 (= 0.8).

The complex viscosity is reported in Figs. 10(e) and 10(f) versus the volume fraction ϕ for the two values of Ca_0 under consideration. Consistently with the results described so far, η' follows the trend displayed by $|\mu_{sp}|^{amp}$ for both high and low Ca_0; in particular, η' is higher for low Ca_0 than for high Ca_0, confirming once more the shear thinning with deformability of elastic objects. Furthermore, η' at low f_{in} (= 0.05) is always higher than at high f_{in} (= 0.5) for each ϕ, while this trend is opposite in η'', which always higher at high f_{in} than those at low f_{in}. Overall, conditions of small Ca_0 and high f_{in} are those to lead to the largest η''.

Thurston[76] adopted the metrics of viscoelasticity discussed in this work, i.e., $\eta^* = \eta' - i\eta''$ (23), and measured the value of η^* of normal human blood (i.e., suspension of RBCs in the plasma) for varying amplitude of the shear rates (or velocity gradient) at a temperature of 25 °C and with concentrations ranging from 0 to 100%. The measurements were carried out at a frequency of 10 Hz, corresponding to $f_{in} \approx 0.25$ in this study. The experimental results showed that for volume fractions above 20% ($\phi \geq 0.2$) and shear rates less than 2 s^{-1}, corresponding to $Ca_0 \approx 2.4 \times 10^{-3}$ in our study ($a_0 = 4$ μm and $G_s = 4$ μN/m are assumed here), the elastic component η'' increased with ϕ approximately cubically (i.e., $\eta'' \propto \phi^3$) while the viscous component η' increases exponentially. Such dramatical increases in both metrics (η' and η'') are seen for low shear rates, which potentially causes the shear-thinning character of the blood[2]. In our study, the minimum shear rate condition is ≈ 42 s^{-1} ($Ca_0 = 0.05$), which is still over 20 times greater than the experimental condition of Thurston[76], and the increase of η' and η'' as a function of ϕ (see Figs. 10e and 10f) are more moderate than in the experiment. For precise comparison with experimental data, modeling of aggregation and disaggregation of RBCs would also be important.

E. Membrane tension under oscillatory shear flow

Finally, we also investigate the maximal in-plane principal tension T_1 ($\geq T_2$) and the isotropic tension $T_{iso}(= T_1 + T_2)/2$ in the deformed RBC, and display the results in Fig. 11. We indicate the spatial-temporal average of those tensions as $\langle T_1\rangle$ and $\langle T_{iso}\rangle$, which are computed using equation (8). It is known that these tensions monotonically increase with Ca, as observed in narrow rectangular microchannels[83]. Similarly to the normal
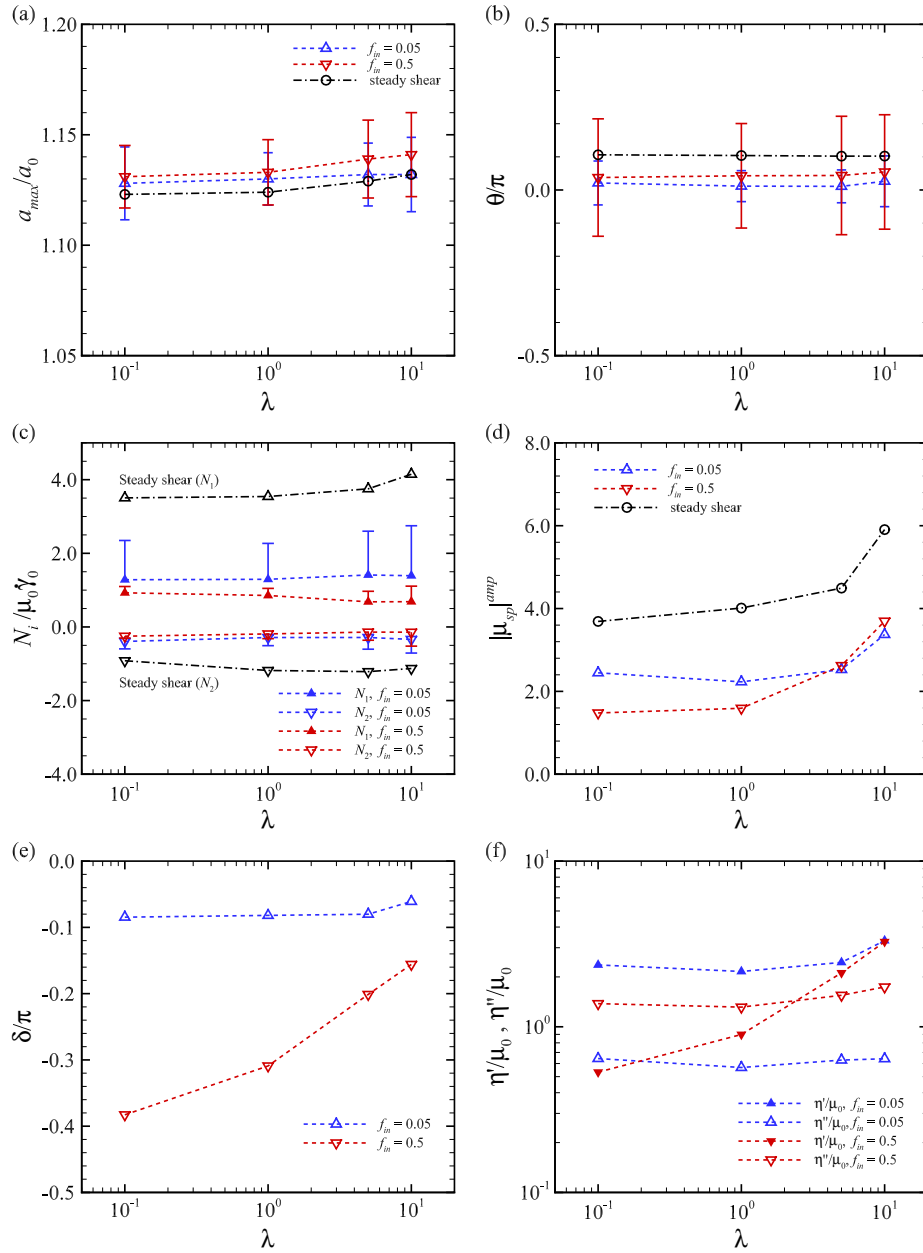
FIG. 6. (a) Spatial-temporal average of the deformation index $\langle a_{max} \rangle / a_0$, (b) orientation angle $\langle \theta \rangle / \pi$, (c) the first and second normal stress differences $\langle N_i \rangle / \mu_0 \dot{\gamma}_0$ ($i = 1$ and 2), (d) amplitude $|\mu_{sp}|^{amp}$, (e) phase difference δ / π, and (f) complex viscosity η' / μ_0 and η'' / μ_0 as a function of viscosity ratio λ (= 0.1, 1, 5 and 10). The results obtained under steady shear flow at each λ are also displayed in (a)–(d) as black dash-dot lines. The results are obtained with $\phi = 0.41$ and $Ca_0 = 0.05$ for relatively low and high shear frequencies, $f_{in} = 0.05$ and $f_{in} = 0.5$.

stress differences $\langle N_i \rangle$, the values of $\langle T_i \rangle$ also decrease with f_{in}, independently of ϕ (Figs. 11a and 11b), clearly indicating the decrease of the RBC deformation and a reduction in their hydrodynamic interactions. Indeed, the magnitude of $|\langle T_i \rangle|$ decreases for all f_{in}, compared to those in a steady shear flow, with the maximum principal tension $\langle T_1 \rangle$ being much lower especially in the dilute condition ($\phi = 0.11$). A frequency-dependent decrease of the membrane tensions is also found for all ϕ both for $Ca_0 = 0.05$ and $Ca_0 = 0.8$ (Figs. 11c and 11d, respectively).

The state of membrane tension is further investigated for different viscosity ratios λ, the results shown in Fig. 11(e). Compared with the previous results of single RBC in Refs. 83 and 84, the similarities or discrepancies in the values of $\langle T_i \rangle$ for different λ arise here from the different input frequencies f_{in}. The observations above about the reduction in membrane tension with the oscillations are valid also for the different values of λ examined. Considering these results shown in Fig.11, SAOS flow basically impedes the deformation of individual RBCs as well as the magnitude of fluid-membrane
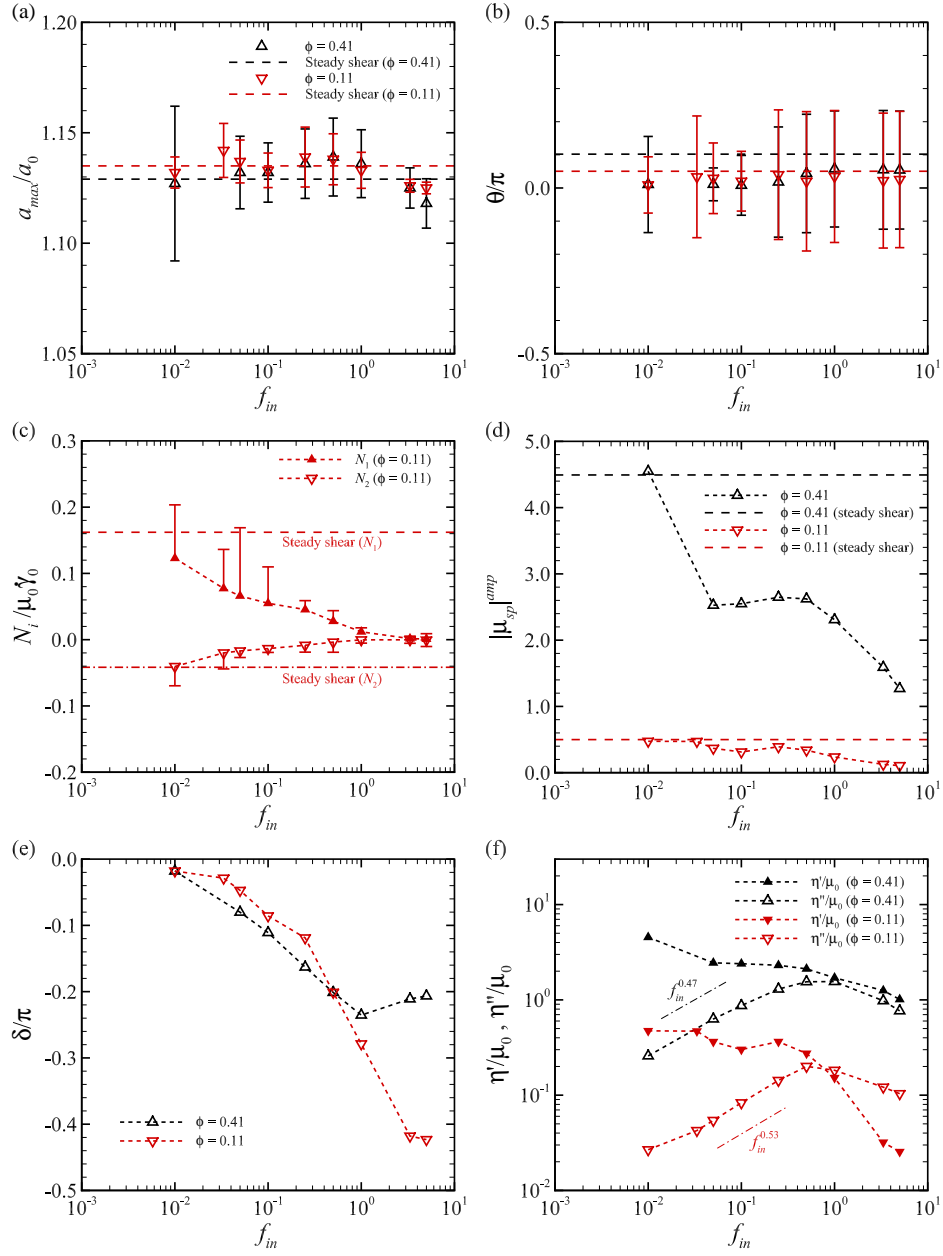
FIG. 7. (a) Spatial-temporal average of the deformation index $\langle a_{max} \rangle / a_0$, (b) orientation angle $\langle \theta \rangle / \pi$, (c) the first and second normal stress differences $\langle N_i \rangle / \mu_0 \dot{\gamma}_0$ ($i = 1$ and 2), (d) amplitude $|\mu_{sp}|^{amp}$, (e) phase difference δ / π, and (f) complex viscosity η' / μ_0 and η'' / μ_0 as a function of f_{in} for dilute ($\phi = 0.11$) and dense ($\phi = 0.41$) suspensions. The results obtained under steady shear flow are displayed in panels (a)–(d) with dashed lines. The results are obtained with $Ca_0 = 0.05$, and $\lambda = 5$.

interactions, resulting in a lower specific viscosity and first and second normal stress differences than in steady shear flow (Figs. 7c and 7d).

Overall, the input frequency results to be the main parameter affecting the tension of the RBC membrane. Although we could not observe any particular frequency-induced variation of the deformation of the RBCs in terms of the index $\langle a_{max} \rangle / a_0$, the membrane tension is strongly affected by the input frequency. Therefore, the full viscoelastic behavior of RBC suspensions cannot be simply estimated by the geomet-

rical properties of individual deformed RBCs, but it should include the state of the membrane tension, which appears to be strongly related to the normal-stress differences (see Figs. 11a and 11b).

IV. CONCLUSIONS

We have performed numerical simulations of dense suspension of RBCs under SAOS for a wide rage of shear frequen-
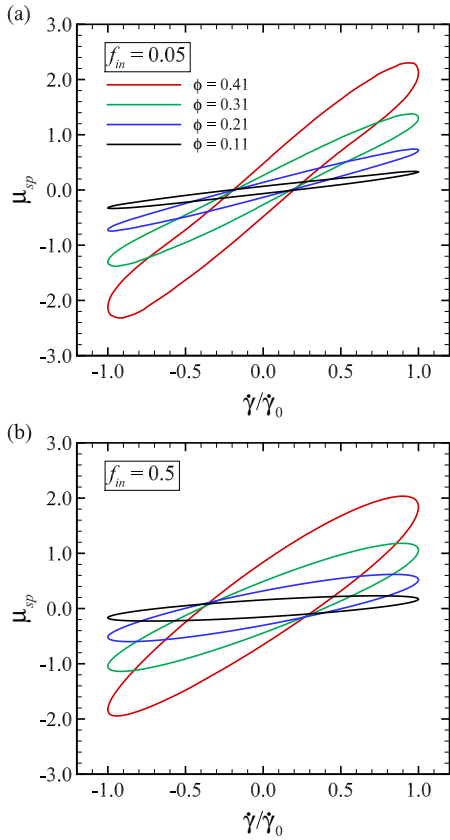
FIG. 8. Lissajous-Bowditch plots of μ_{sp} versus $\dot{\gamma}/\dot{\gamma}_0$ at $Ca_0 = 0.8$ for different ϕ at (a) f_{in}=0.05 and (b) f_{in} = 0.5. The results are obtained with viscosity ratio $\lambda = 5$.

cies f_{in}, and quantified the viscoelastic character of the bulk suspension by its complex viscosity; this is defined in terms of the amplitude of the particle stress and the phase difference between the output particle stress and the sinusoidal applied shear (see Eq. 25). The flow is assumed to be inertialess, with the fluids inside and outside the RBCs modeled as Newtonian. The role of the viscosity ratio λ, the volume fraction of the RBCs ϕ, and the Ca_0 on the complex viscosity have been evaluated and discussed.

The first important question we focused on is whether the cell deformation might be enhanced by varying the oscillatory frequency. Although frequency-induced deformation can be found both in dense and dilute conditions, especially for the intermediate range of frequencies, $0.05 \leq f_{in} \leq 1$ corresponding to 2.1 Hz $\leq$ f $\leq$ 42 Hz for $Ca_0 = 0.05$ (≈ 42 s^{-1} assuming the reference radius of $a_0 = 4$ μm and the surface shear elastic modulus of $G_s = 4$ μN/m), the differences with the deformations in steady shear flow are always less than 1%. Thus, enhancement of cell deformation under oscillatory shear is unlikely to occur for RBCs. Previous numerical analysis of a single spherical capsule, whose membrane follows the neo-Hookean (NH) constitutive law (i.e., strain-softening property), demonstrated that frequency-dependent deformations become evident for high Ca and large values of λ[19], specifically $Ca = 2.0$ and $\lambda = 10$, with a 26% de-

formation increase observed at $f_{in} = 0.01$. Our results, however, show that even for relatively large Ca_0 (= 0.8), the cell deformation by oscillatory shear flow is very limited for biconcave capsules, which is possibly due to the SK law (i.e., strain-hardening membrane property). Focusing on biological systems, the oxygen-dependent regulation of RBC properties should be taken into considerations[16]. For instance, it is known that the elongation of RBCs in response to shear stresses increases as oxygen tension is decreased[17]. Thus, it will be interesting to study whether deformation of RBCs under pulsatile flows results in passive regulation for oxygen transport. Differently from what observed for the cell deformation, the tension of the membrane decreases significantly with the input frequency, also resulting in a decrease of the normal stress differences. This result suggests that the viscoelastic character of RBC suspensions can be fully understood only by accounting for the state of the membrane tension.

Our next question is how the bulk suspension rheology is altered in oscillatory flows when compared to the case of steady shear flow, where most experimental measures are taken. As f_{in} increases, η' gradually decreases, while η'' attains its maximum value at frequency $f_{in} = 0.5$ corresponding to f = 21 Hz (Fig. 7f). A similar trend was reported for a single spherical capsule with NH law in Matsunaga and Imai[48], where η'' was shown to reach its maximum at $f_{in} = 0.2$. Interestingly, the local maximum f_{in}^{max} (= 0.5) remains the same in dilute condition ($\phi = 0.11$) for the RBC suspensions considered here (Fig. 7f); therefore, the discrepancy in the frequency of the maximum η'' with the previous numerical study by Matsunaga and Imai[48] might be due to the different membrane constitutive law or the capsule shape rather than an effect of the volume fraction. Furthermore, the curves obtained here for η'' are qualitatively similar to those in Oldroyd-B fluids[78,79], whose N_2 is however null. While the ratio $-N_2/N_1$ is not exactly equal to 0.5 as typically observed in liquid crystals consisting of rod-like polymer solution[78], it has the same order of magnitude $O(-\langle N_2 \rangle/\langle N_1 \rangle) = 10^{-1}$, and it is almost independent of the volume fraction ϕ. Overall, SAOS flow basically impedes the deformation of individual RBCs as well as the magnitude of fluid-membrane interactions (Fig.11), resulting in a lower specific viscosity and first and second normal stress differences than in steady shear flow (Figs. 7c and 7d).

This study provides the first conclusive evidence of oscillatory rheology of suspension of RBCs in SAOS. Although it is known that the RBC deformation alone is sufficient to give rise to shear-thinning[42], the resulting complex viscosity shown in the Fig. 7(f) weakly depends on the frequency-modulated deformations or orientations of individual RBCs (Figs. 7a and 7b, respectively), but rather depends on combinations of the frequency-dependent amplitude $|\mu_{sp}|^{amp}$ and phase difference δ (Figs. 7d and 7e, respectively). Effects of particle deformability, inertia, and LAOS on the viscoelastic character in suspensions of RBCs will be reported in a future study. A physiological interpretation for the local maximum of the η'' viscosity at a frequency of ≈ 21 Hz is still missing. Since this is 20 times higher than the physiological heart beat (≈ 1 Hz), such high frequency hydrodynamic interactions
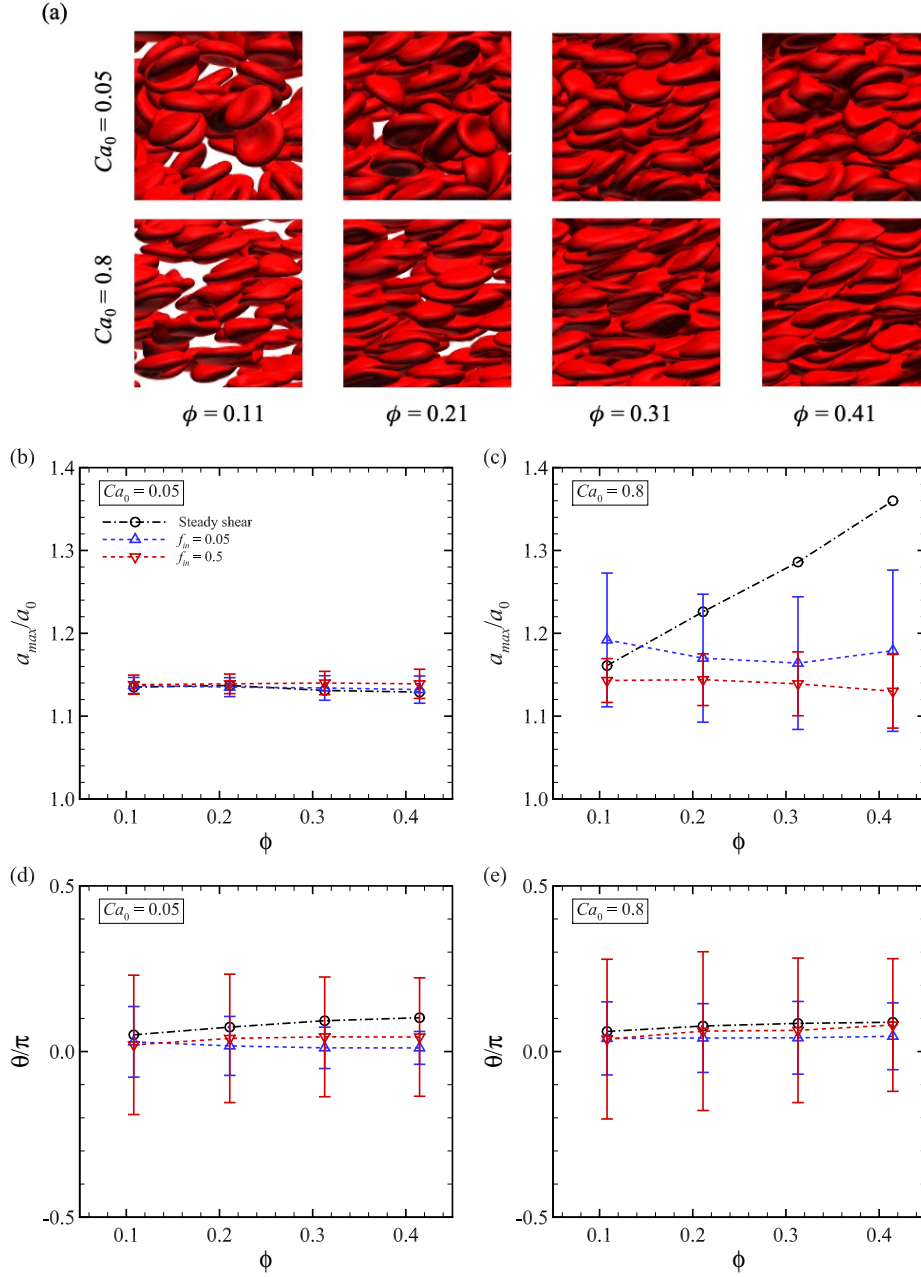
FIG. 9. (a) Snapshots from our numerical results of suspensions with different ϕ=0.11 and 0.41 at imposed shear frequency f_{in} = 0.5. The top raw shows the data at the lowest Ca_0 = 0.05 and the bottom raw those at the highest Ca_0= 0.8. (b and c) Spatial-temporal average of the deformation index $\langle a_{max}\rangle/a_0$, and (d and e) orientation angle $\langle\theta\rangle/\pi$ as function of ϕ for two values of f_{in} (0.05 and 0.5). The left column (panels b, and d) displays the results for Ca_0 = 0.05, and the right column (c, and e) those for Ca_0 = 0.8. The results are obtained for viscosity ratio λ = 5.

may only occur in local vascular areas, e.g., aneurisms, or in an artificial blood pumps. Thus, in the future, it will be interesting to also study whether such high-frequency oscillations can induce or delay blood clots.

The values of the dimensional frequency studied in this work f$(= f_{in}\dot\gamma_0 = f_{in}Ca_0\{G_s/(\mu_0 a_0)\})$ are estimated using G_s = 4 μN/m (see also Figure 12 in Takeishi et al. [11]), which is determined by fitting the lengths of stretched RBCs by optical

tweezers at steady state[85]. Thus, the exact values of the frequency depend on the estimation of G_s, which varies with the membrane constitutive laws and is also sensitive to different experimental methodologies, e.g., atomic force microscopy, micropipette aspiration and etc[86]. Direct comparison with experiments is therefore not trivial and left as a future study.

Existing works on oscillatory rheology focus on building macroscale models for dilute suspensions: soft particle
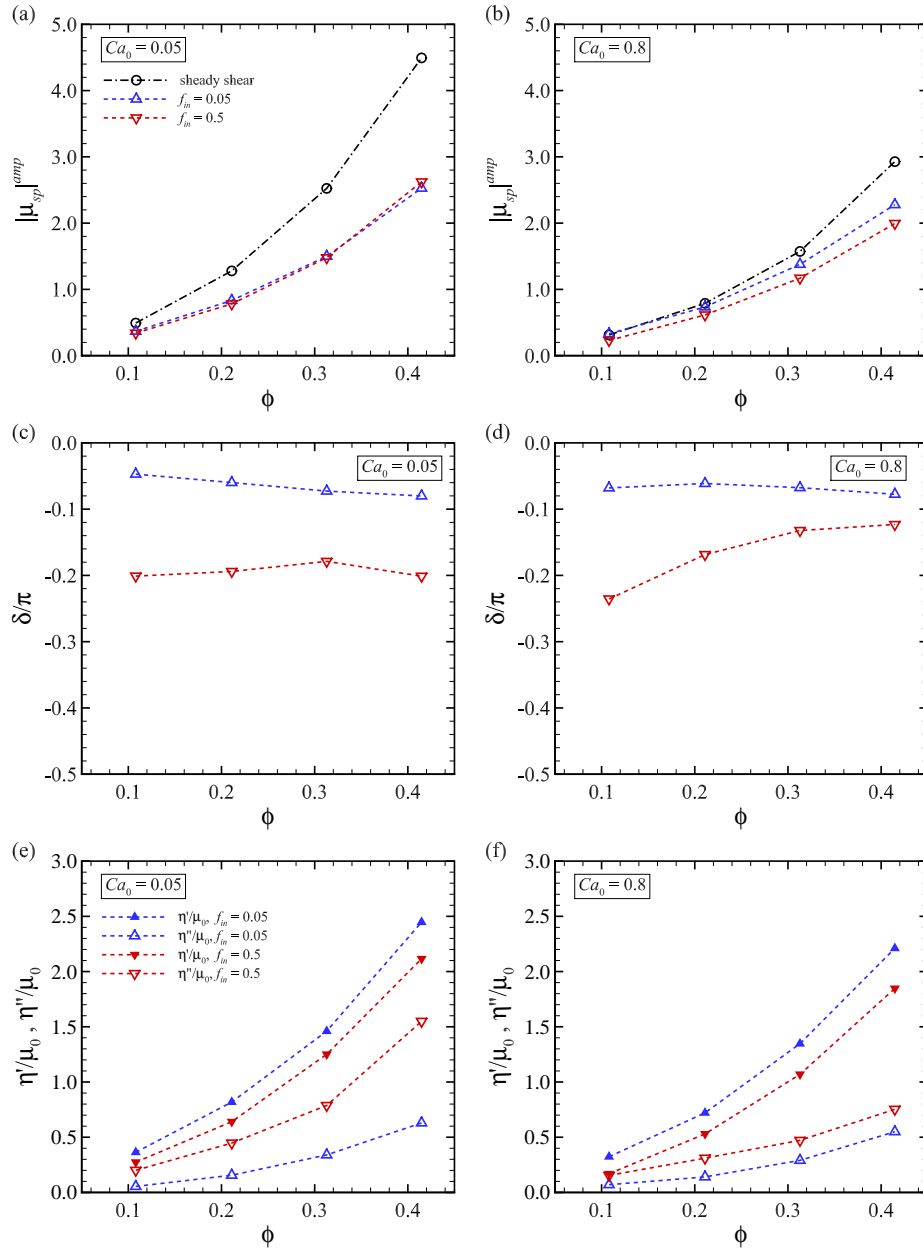
FIG. 10. (a and b) Spatial-temporal average of the amplitude of the specific viscosity $|\mu_{sp}|^{amp}$, (c and d) phase difference between applied shear and corresponding stress δ/π, and (e and f) complex viscosity η'/μ_0 and η''/μ_0 as function of the volume fraction ϕ and the oscillatory frequency f_{in} (= 0.05 and 0.5). The left column (panels a, c, and e) displays the results for $Ca_0 = 0.05$, and the right column (b, d, and f) those for $Ca_0 = 0.8$. The results are obtained for viscosity ratio $\lambda = 5$.

glasses[44], viscoelastic particles[45], bubbles[46], vesicles[47], and NH capsule[48]. Although a suspension of particles can be described as a continuum at length scales large compared to the size of the constituent particles, none of these works successfully derived constitutive equations for the oscillatory rheology of dense suspensions. Misbah[37] derived an equation to describe the suspension viscosity μ_{eff} in the tank-treading regime under the assumption of small deformations of vesicles in steady shear flow: $(\mu_{eff} - \mu_0)/(\phi\mu_0) = 2.5 - \mathscr{A}(23\lambda + 32)/(16\pi)$, where $\mathscr{A}$ is the excess area. The next challenge

will therefore be extending the applicability of such models to cover a wide range of volume fractions and large deformations of RBCs. Our numerical results and quantitative model analysis of the viscoelastic property of dense suspensions of RBCs will be also helpful to build more sophisticated non-Newtonian constitutive laws that consider multi-scale dynamics, and to gain insights not only into the passive cellular flow in physiological systems[1–4], but also into the design of novel artificial blood pumps[15]. We hope that our numerical results will stimulate further numerical and experimental stud-
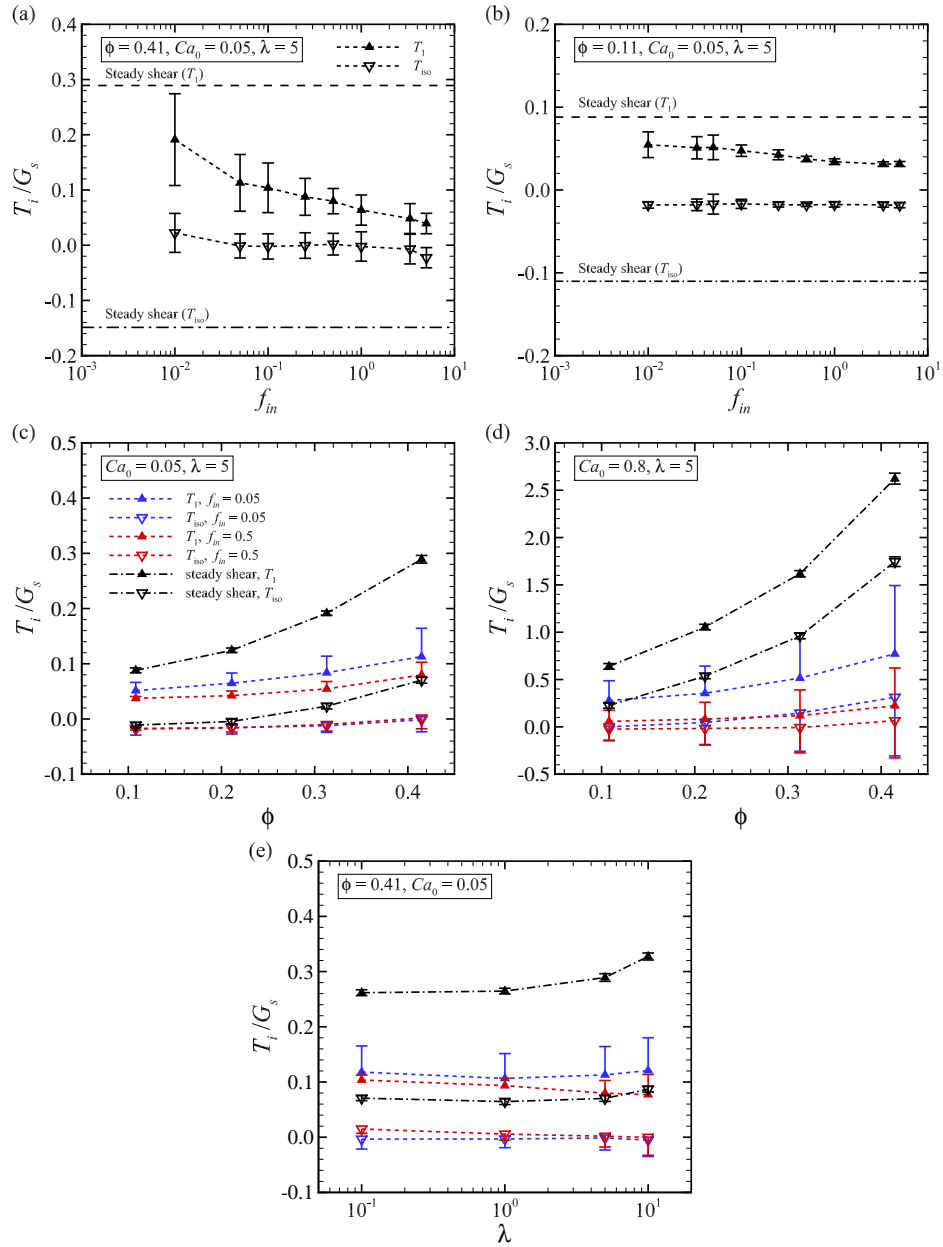
FIG. 11. (a and b) Spatial-temporal average of the first and isotropic tensions (T_1 and T_{iso}, respectively) as a function of f_{in} for (a) dense ($\phi = 0.41$) and (b) dilute ($\phi = 0.11$) conditions. The results are obtained for SAOS ($Ca_0 = 0.05$). In (c) and (d), the membrane tensions are shown as function of ϕ and f_{in} (= 0.05 and 0.5) for (c) $Ca_0 = 0.05$ and (d) $Ca_0 = 0.8$. The results shown in (a)–(d) are obtained for $\lambda = 5$. (e) The membrane tensions as function of the viscosity ratio λ and f_{in} (= 0.05 and 0.5) for dense condition ($\phi = 0.41$). The result in (e) is obtained for SAOS ($Ca_0 = 0.05$).

ies, able to shed light on the complex interplay between cellular dynamics and oxygen transport in the microcirculation.

ACKNOWLEDGMENTS

AUTHOR DECLARATIONS

Conflict of Interest

The authors report no conflict of interest.

Author Contributions

Naoki Takeishi: Conceptualization (equal); Funding acquisition (lead); Data curation (lead); Formal analysis (lead); Investigation (lead); Methodology (lead); Resources (lead); Software (lead); Validation (lead); Visualization (lead); Writing - original draft (lead); Writing - review & editing (equal). **Marco Edoardo Rosti:** Conceptualization (equal); Funding acquisition (supporting); Data curation (supporting); Formal analysis (supporting); Investigation (supporting); Methodology (supporting); Validation (supporting); Writing - review & editing (equal). **Naoto Yokoyama:** Conceptualization (equal); Data curation (supporting); Formal analysis (supporting); Investigation (supporting); Methodology (supporting); Validation (supporting); Writing - review & editing (equal). **Luca Brandt:** Conceptualization (lead); Funding acquisition (lead); Data curation (supporting); Formal analysis (supporting); Investigation (supporting); Methodology (supporting); Validation (supporting); Writing - review & editing (lead).

Appendix A: Effect of the domain size

The presence of walls bounding the suspension causes a finite CDPL. We quantify the thickness of the CDPL as done in a previous work[59]. The result is shown in Fig. 12(a), where the thicknesses of the CDPL at $\phi = 0.21$ and $f_{in} = 1$ are investigated for different domain heights H (= $7.5a_0$, $10a_0$, and $12.5a_0$). We observe that the change in CDPL between the present height ($H = 10a_0$) and a larger one ($H = 12.5a_0$) $|CDPL_{H=10a_0}/CDPL_{H=12.5a_0} - 1|$ is less than 3%, so we can conclude that the thickness of CDPL remains almost the same for $H \geq 10a_0$.

Effective volume fraction profiles along the domain height ϕ_y are also shown at the minimum and maximum f_{in} (= 0.01 and 5) for $\phi = 0.41$ in Fig. 12(b). The data show that ϕ_y is slightly greater than ϕ (or Hct_D), i.e., $\phi_y > \phi$, near the wall regions, with no big differences observed for the two f_{in}. We also evaluate the value of several observables (the phase difference δ, the amplitude of the specific viscosity $|\mu_{sp}|^{amp}$, and the moduli of the complex viscosity η'/μ_0 and η''/μ_0) for different values of the wall-to-wall distance H, whose results with the corresponding relative errors are listed in table I. Since the difference between the case with the largest height ($H = 12.5a_0$) and our reference case are less than 2% for all
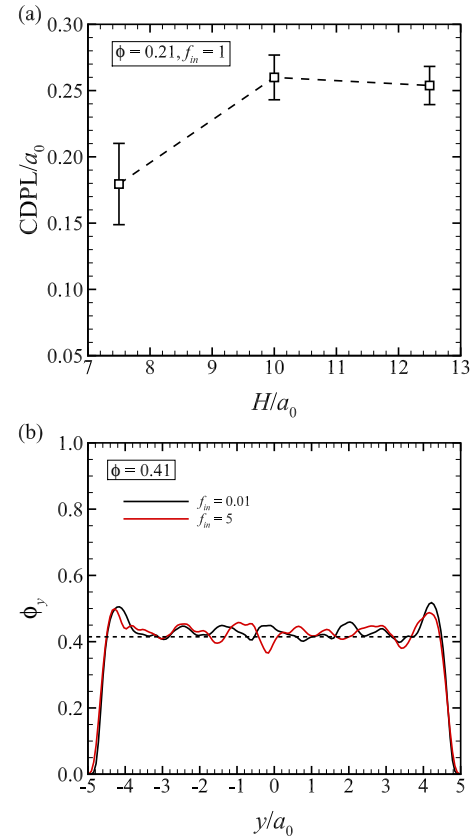

FIG. 12. (a) Thickness of the CDPL for different domain height H/a_0 (= 7.5, 10, and 12.5) at $\phi = 0.21$, $Ca_0 = 0.4$, and $f_{in} = 1$. The error bars represent the standard deviation over time. (b) The effective volume fraction profile ϕ_y along the domain height y at the minimum and maximum frequency f_{in} (= 0.01 and 5, respectively) for a channel height $H = 10a_0$, where the dashed line denotes the volume fraction (or Hct_D) $\phi = 0.41$ (dashed line). The results are obtained on the fully developed flow and pertain the simulations with $\lambda = 5$.

the quantities, the results presented in this study are all obtained with the domain height $H = 10a_0$, as also done in our previous numerical analysis[11].

Appendix B: Stokes boundary layer

In the laminar regime, a boundary layer generated by the harmonic oscillations is denoted by a viscous length δ_S or Stokes boundary layer (SBL)[87]. A conventional viscous length δ_S is defined using the kinematic viscosity ν of the (external) fluid; $\delta_S = \sqrt{2\nu/\omega}$. Therefore, a non-dimensional length can be defined as $\delta_S^* = \delta_S/a_0 = 1/\sqrt{\pi Re f_{in}}$. We quantify the distance δy_{max} at $Re = 0.2$ along the wall-normal coordinate y where the effective volume fraction profile ϕ_y is maximum, and compare with δ. The result is shown in Fig. 13. All numerical results of δy_{max} are smaller than or comparable to the estimated SBL. Furthermore, the result of δy_{max} at $Re = 0.2$ is consistent with that obtained with smaller Re (= 0.05). The distance δy_{max} is independent of f_{in}, indicating

TABLE I. Effect of the domain height H on the phase difference δ, amplitude of the specific viscosity $|\mu_{sp}|^{amp}$, and moduli of the complex viscosity (η'/μ_0 and η''/μ_0). The error parameter $\varepsilon(\chi)$ is calculated based on $H = 10a_0$. The simulations are performed at $\phi = 0.21$, $Ca_0 = 0.4$, $\lambda = 5$, and $f_{in} = 1$.

Height H	$7.5a_0$	$10a_0$ (reference)	$12.5a_0$
Number of RBCs	258	344	442
δ/π	-0.19032	-0.19069	-0.18874
$\varepsilon(\delta/\pi)$	0.00189	-	0.01021
$|\mu_{sp}|^{amp}$	0.59599	0.53463	0.54107
$\varepsilon(|\mu_{sp}|^{amp})$	0.11477	-	0.01205
η'/μ_0	0.49259	0.44153	0.44871
$\varepsilon(\eta'/\mu_0)$	0.11563	-	0.01626
η''/μ_0	0.33550	0.30146	0.30235
$\varepsilon(\eta''/\mu_0)$	0.11292	-	0.00297

FIG. 14. The time-averaged distance of neighboring membrane nodes $\langle\Delta_{node}\rangle/\Delta x_{LBM}$ as a function of ϕ, where Δx_{LBM} is the mesh size of the LBM. The results are obtained with $Ca = 0.05$, viscosity ratio $\lambda = 5$, and frequency $f_{in} = 0.5$.

Appendix D: Discrete Fourier transform

The peak frequency and amplitude of the output signal, the specific viscosity μ_{sp}, and of the imposed shear rate $\dot{\gamma}$ are calculated by the discrete Fourier transform (DFT), defined as:

$$X(f_k) = \sum_{j=0}^{n-1} x(t_j)\exp(-i2\pi jk/n), \qquad (D1)$$

where $X(f_k)$ is the Fourier coefficient of the variable x for the k-th mode, and n is the number of data points. Considering only the signal dominant component of frequency f_p, the one of the imposed shear as shown below, we can write the input and output signals as $\dot{\gamma}(t) \approx \dot{\gamma}_0\cos(2\pi f_p t + \Theta_{\dot{\gamma}})$ and $\mu_{sp}(t) \approx |\mu_{sp}|^{amp}\cos(2\pi f_p t + \Theta_{\mu_{sp}})$, with the phase difference δ ($-\pi/2 \le \delta \le 0$) expressed as $\delta = \Theta_{\mu_{sp}} - \Theta_{\dot{\gamma}}$. The phases Θ ($= \Theta_{\dot{\gamma}}$ or $\Theta_{\mu_{sp}}$) can be defined as the angle between the real and imaginary parts of the Fourier coefficient $X(f_p)$ at the peak frequency f_p of $\dot{\gamma}(t)$ or $\mu_{sp}(t)$:

$$\Theta = \text{atan2}(\text{Im}(X(f_p)), \text{Re}(X(f_p))). \qquad (D2)$$

Indeed, the calculated peak frequencies of $\dot{\gamma}$ and μ_{sp} coincide with the input strain frequency $f_{in}(= \text{f}/\dot{\gamma}_0)$ as shown in Fig. 15.
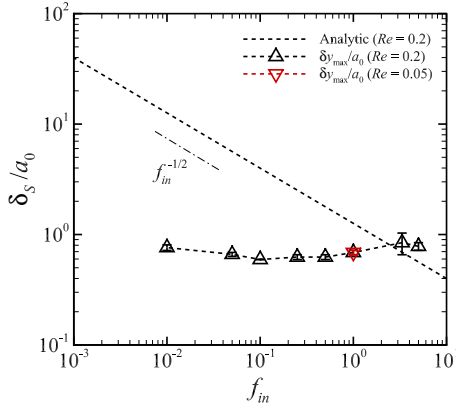

FIG. 13. Time average of the distance δy_{max} at $Re = 0.2$ along the domain height y when the effective volume fraction profile ϕ_y is maximized, where the dashed line denotes the SBL layer thickness δ_S at $Re = 0.2$. The result of δy_{max} at $Re = 0.05$ and $f_{in} = 1$ is also superposed. The results are obtained on the fully developed flow and pertain the simulations with $\lambda = 5$.

that the CDPL is irrelevant to the SBL.

Appendix E: Effect of wave periods on the solutions by DFT analysis

The accuracy of the analysis is important especially for small values of δ because the complex modulus is proportional to $\sin\delta \approx \delta$ for $\delta \ll 1$. We have therefore checked the effect of the number of wave periods used for the input and output signals in the DFT analysis: δ/π, $|\mu_{sp}|^{amp}$, η', η''. Specifically, we have computed these values for a number of periods ranging from 5 to 30, where each output wave is resolved by a sufficiently large number of discrete points

Appendix C: Distance between neighboring membrane nodes

We further investigated the distance between neighboring membrane nodes. The result of time-averaged distance of neighboring membrane nodes $\langle\Delta_{node}\rangle$ for different volume fractions ϕ is shown in Fig. 14. The result is obtained with $Ca = 0.05$, viscosity ratio $\lambda = 5$, and frequency $f_{in} = 0.5$. Even at the highest volume fraction $\phi = 0.41$, the average distance still maintains over two fluid lattices. Thus, at least for $\phi \le 0.41$, our coupling of LBM and IBM successfully resolve the distance between neighboring membrane nodes.
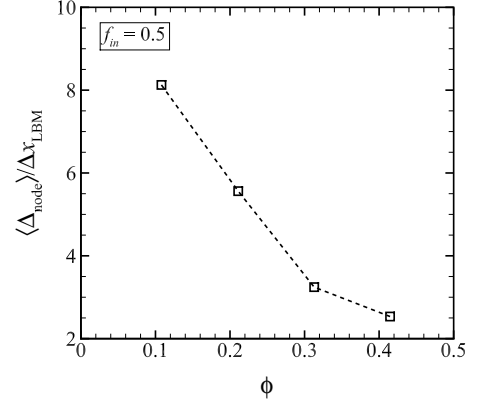
TABLE II. Effect of the number of wave periods used in the DFT analysis on the phase difference δ, amplitude of the specific viscosity $|\mu_{sp}|^{amp}$, and moduli of the complex viscosity (η'/μ_0 and η''/μ_0). The error parameter $\varepsilon(\chi)$ is defined as $\varepsilon(\chi) = |\chi/\chi_{ref} - 1|$, where the subscript ref indicates the reference values. The simulations are performed at $\phi = 0.41$, $Ca = 0.05$, $\lambda = 5$, and $f_{in} = 0.05$.

| Number of wave periods	5	10	15	20	25	30 (ref)
δ/π	-0.07956	-0.08127	-0.08117	-0.08080	-0.08045	-0.08014
$\varepsilon(\delta/\pi)$	0.00730	0.01400	0.01283	0.00818	0.00382	-
$|\mu_{sp}|^{amp}$	2.76387	2.43931	2.46789	2.49496	2.51260	2.52682
$\varepsilon(|\mu_{sp}|^{amp})$	0.09381	0.03463	0.02332	0.01261	0.00563	-
η'/μ_0	2.67798	2.36025	2.38808	2.41501	2.43278	2.44715
$\varepsilon(\eta'/\mu_0)$	0.09433	0.03551	0.02414	0.01313	0.00587	-
η''/μ_0	0.68364	0.61603	0.62254	0.62654	0.62830	0.62950
$\varepsilon(\eta''/\mu_0)$	0.08600	0.02141	0.01107	0.00470	0.00191	-
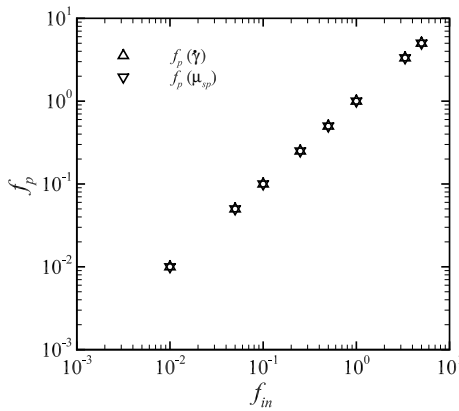
FIG. 15. The peak frequency f_p of the input shear rate $\dot{\gamma}(t)$ versus the peak frequency of the output specific viscosity $\mu_{sp}(t)$ calculated by the DFT analysis as a function of shear rate frequency f_{in} ($= f/\dot{\gamma}_0$). The results pertain the simulations with $\phi = 0.41$, $\lambda = 5$, and $Ca_0 = 0.05$.

(≥ 100). The values and errors obtained with respect to the data from the longest signal (30 periods) are summarised in table II. All errors decrease as the number of wave periods increases. For a reasonable analysis, we deem necessary to use at least 10 periods, which gives a difference lower than 4% with respect to using the full 30 wave periods.

[1] S. Chien, S. Usami, R. J. Dellenback, and M. I. Gregersen, "Blood viscosity: influence of erythrocyte deformation," Science **157**, 827–829 (1967).

[2] S. Chien, "Shear dependence of effective cell volume as a determinant of blood viscosity," Science **168**, 977–979 (1970).

[3] G. R. Cokelet and H. J. Meiselman, "Rheological comparison of hemoglobin solutions and erythrocyte suspensions," Science **162**, 275–277 (1968).

[4] H. L. Goldsmith and R. Skalak, "Hemodynamics," Ann. Rev. Fluid Mech. **7**, 213–247 (1975).

[5] H. Schmid-Schönbein and R. Wells, "Fluid drop-like transition of erythrocytes under shear," Science **165**, 288–291 (1969).

[6] T. M. Fischer, M. Stöhr-Liesen, and H. Schmid-Schönbein, "The red cell as a fluid droplet: tank tread-like motion of the human erythrocyte membrane in shear flow," Science **202**, 894–896 (1978).

[7] M. Abkarian, M. Faivre, and A. Viallat, "Swinging of red blood cells under shear flow," Phys. Rev. Lett. **98**, 188302 (2007).

[8] L. Lanotte, J. Mauer, S. Mendez, D. A. Fedosov, J.-M. Fromental, V. Claveria, F. Nicoul, G. Gompper, and M. Abkarian, "Red cells' dynamic morphologies govern blood shear thinning under microcirculatory flow conditions," Proc. Natl. Acad. Sci. USA. **113**, 13289–13294 (2016).

[9] D. Cordasco, A. Yazdani, and P. Bagchi, "Comparison of erythrocyte dynamics in shear flow under different stress-free configurations," Phys. Fluids **26**, 041902 (2014).

[10] K. Sinha and M. D. Graham, "Dynamics of a single red blood cell in simple shear flow," Phys. Rev. E. **92**, 042710 (2015).

[11] N. Takeishi, M. E. Rosti, Y. Imai, S. Wada, and L. Brandt, "Haemorheology in dilute, semi-dilute and dense suspensions of red blood cells," J. Fluid Mech. **872**, 818–849 (2019).

[12] P. M. Vlahovska, T. Podgorski, and C. Misbah, "Vesicles and red blood cells in flow: from individual dynamics to rheology," C. R. Physique. **10**, 775–789 (2009).

[13] R. Skalak and P.-I. Branemark, "Deformation of red blood cells in capillaries," Science **164**, 717–719 (1969).

[14] A. G. Koutsiaris, S. V. Tachmitzi, and N. Batis, "Wall shear stress quantification in the human conjunctival pre-capillary arterioles in vivo," Microvasc. Res. **85**, 34–39 (2013).

[15] S. Deutsch, J. M. Tarbell, K. B. Manning, G. Rosenberg, and A. A. Fontaine, "Experimental fluid mechanics of pulsatile artificial blood pumps," Annu. Rev. Fluid Mech. **38**, 65–86 (2006).

[16] K. Parthasarathi and H. H. Lipowsky, "Capillary recruitment in response to tissue hypoxia and its dependece on red blood cell deformability," Am. J. Physiol. Heart Circ. Physiol. **46**, H2145–H2157 (1999).

[17] H. S. Wei, H. Kang, I.-Y. D. Rasheed, S. Zhou, N. Lou, A. Gershteyn, E. D. McConnell, Y. Wang, K. E. Richardson, A. F. Palmer, C. Xu, J. Wan, and M. Nedergaard, "Erythrocytes are oxygen-sensing regulators of the cerebral microcirculation," Neuron **91**, 851–862 (2016).

[18] S. Zhou, M. Giannetto, J. DeCourcey, H. Kang, N. Kang, Y. Li, S. Zheng, H. Zhao, W. R. Simmons, H. S. Wei, D. M. Bodine, P. S. Low, M. Nedergaard, and J. Wan, "Oxygen tension-mediated erythrocyte membrane interactions regulate cerebral capillary hyperemia," Sci. Adv. **5**, eaaw4466 (2019).

[19] D. Matsunaga, Y. Imai, T. Yamaguchi, and T. Ishikawa, "Deformation of a spherical capsule under oscillating shear flow," J. Fluid Mech. **762**, 288–301 (2015).

[20] T. Nakajima, K. Kon, N. Maeda, K. Tsunekawa, and T. Shiga, "Deformation response of red blood cells in oscillatory shear flow," Am. J. Physiol. **259**, H1071–H1078 (1990).

[21] S. Recktenwald, K. Graesse, F. M. Maurer, T. John, S. Gekle, and C. Wagner, "Red blood cell shape transitions and dynamics in time-dependent capillary flows," Biophys. J. **121**, 23–36 (2022).

[22] N. Watanabe, H. Kataoka, T. Yasuda, and S. Takatani, "Dynamic deformation and recovery response of red blood cells to a cyclically reversing shear flow: effects of frequency of cyclically reversing shear flow and shear stress level," Biophys. J. **91**, 1984–1998 (2006).

[23] H. Noguchi, "Dynamic modes of red blood cells in oscillatory shear flow," Phys. Rev. E **81**, 061920 (2010).

[24] X. Li, Z. Peng, H. Lei, M. Dao, and G. E. Karniadakis, "Probing red blood cell mechanics, rheology and dynamics with a two-component multi-scale model," Phil. Trans. R. Soc. A **372**, 20130389 (2014).

[25] D. Cordasco and P. Bagchi, "Dynamics of red blood cells in oscillating shear flow," J. Fluid Mech. **800**, 484–516 (2016).

[26] Q. Zhu and R. J. Asaro, "Response modes of erythrocytes in high-frequency oscillatory shear flows," Phys. Fluids **31**, 051901 (2019).

[27] T. M. Squires and T. G. Mason, "Fluid mechanics of microrheology," Annu. Rev. Fluid Mech. **42**, 413–438 (2010).

[28] J. Mewis and N. J. Wagner, "Colloidal suspension rheology," (Cambridge University Press, 2012) Chap. 1 Introduction to colloid science and rheology, Subsec. 1.2.3 Viscoelasticity, pp. 25–30.

[29] T. G. Mason and D. A. Weitz, "Optical measurements of frequency-dependent linear viscoelastic moduli of complex fluids," Phys. Rev. Lett. **74**, 1250–1253 (1995).

[30] N. J. Wagner, "The high-frequency shear modulus of colloidal suspensions and effects of hydrodynamic interactions," J. Colloid Int. Sci. **161**, 169–181 (1993).

[31] R. A. Lionberger and W. B. Russel, "High frequency modulus of hard sphere colloids," J. Rheol. **38**, 1885–1908 (1994).

[32] T. Shikata and D. S. Pearson, "Viscoelastic behavior of concentrated spherical suspensions," J. Rheol. **38**, 601 (1994).

[33] H. Fröhlich and R. Sack, "Theory of the rheological properties of dispersions," Proc. R. Soc. Lond. A **185**, 415–439 (1946).

[34] J. G. Oldroyd, "The elastic and viscous properties of emulsions and suspensions," Proc. R. Soc. Lond. A **218**, 122–132 (1953).

[35] D. Barthès-Biesel, "Motion of a spherical microcapsule freely suspended in a linear shear flow," J. Fluid. Mech. **100**, 831–853 (1980).

[36] J. D. Goddard and C. Miller, "Nonlinear effects in a rheology of dilute suspensions," J. Fluid Mech. **28**, 657–673 (1967).

[37] C. Misbah, "Vacillating breathing and tumbling of vesicles under shear flow," Phys. Rev. Lett. **96**, 028104 (2006).

[38] R. Roscoe, "On the rheology of a suspension of viscoelastic spheres in a viscous liquid," J. Fluid Mech. **28**, 273–293 (1967).

[39] T. Gao, H. H. Hu, and P. P. Castañeda, "Rheology of a suspension of elastic particles in a viscous shear flow," J. Fluid Mech. **687**, 209–237 (2011).

[40] M. E. Rosti, L. Brandt, and D. Mitra, "Rheology of suspensions of viscoelastic spheres: Deformability as an effective volume fraction," Phys. Rev. Fluids **3**, 012301(R) (2018).

[41] M. E. Rosti and L. Brandt, "Suspensions of deformable particles in a Couette flow," J. Non-Newtonian Fluid Mech. **262**, 3–11 (2018).

[42] T. Omori, T. Ishikawa, Y. Imai, and T. Yamaguchi, "Hydrodynamic interaction between two red blood cells in simple shear flow: its impact on the rheology of a semi-dilute suspension." Comput. Mech. **54**, 933–941 (2014).

[43] M. M. Villone, M. E. Rosti, O. Tammisola, and L. Brandt, "Numerical simulations of small amplitude oscillatory shear flow of suspensions of rigid particles in non-newtonian liquids at finite inertia," J. Rheol. **65**, 821–835 (2021).

[44] F. Khabaz, M. Cloitre, and R. T. Bonnecaze, "Structural state diagram of concentrated suspensions of jammed soft particles in oscillatory shear flow," Phys. Rev. Fluids **3**, 033301 (2018).

[45] C. Kammer and P. P. Castañeda, "Theoretical predictions for the rheology of dispersions of highly deformable particles under large amplitude oscillatory shear," J. Fluid Mech. **897**, A1 (2020).

[46] S. Lin, J. Lu, G. Tryggvason, and Y. Zhang, "The effect of fluid shear flow on oscillating bubbly flows," Phys. Fluids **31**, 042110 (2019).

[47] A. Farutin and C. Misbah, "Rheology of vesicle suspensions under combined steady and oscillating shear flows," J. Fluid Mech. **700**, 362–381 (2012).

[48] D. Matsunaga and Y. Imai, "Complex viscosity of dilute capsule suspensions: a numerical study," J. Biomech. Sci. Eng. **15**, 20–00102 (2020).

[49] M. Armstrong, J. Horner, M. Clark, M. Deegan, T. Hill, C. Keith, and L. Mooradian, "Evaluating rheological models for human blood using steady state, transient, and oscillatory shear predictions," Rheol. Acta **57**, 705–728 (2018).

[50] C. Saengow, A. J. Giacomin, and A. S. Dimitrov, "Unidirectional large-amplitude oscillatory shear flow of human blood," Phys. Fluids **31**, 111903 (2019).

[51] J. G. Oldroyd, "Non-Newtonian effects in steady motion of some ideal-ized elastico-viscous liquids," Proc. Natl. Acad. Sci. USA. **245**, 278–297 (1958).

[52] M. Anand, J. Kwack, and A. Masud, "A new generalized Oldroyd-b model for blood flow in complex geometries," Int. J. Eng. Sci **72**, 78–88 (2013).

[53] M. A. Alves, P. J. Oliveira, and F. T. Pinho, "Numerical methods for viscoelastic fluid flows," Annu. Rev. Fluid Mech. **53**, 509–541 (2021).

[54] B. R. Mutlu, J. F. Edd, and M. Toner, "Oscillatory inertial focusing in infinite microchannels," Proc. Natl. Acad. Sci. USA. **115**, 7682–7687 (2018).

[55] J. M. Martel and M. Toner, "Inertial focusing in microfluidics," Ann. Rev. Biomed. Eng. **16**, 371–396 (2014).

[56] G. K. Batchelor, "The stress system in a suspension of force-free particles," J. Fluid Mech. **41**, 545–570 (1970).

[57] R. Skalak, A. Tozeren, R. P. Zarda, and S. Chien, "Strain energy function of red blood cell membranes," Biophys. J. **13**, 245–264 (1973).

[58] C. S. Peskin, "The immersed boundary method," Acta Numer. **11**, 479–517 (2002).

[59] N. Takeishi, Y. Imai, K. Nakaaki, T. Yamaguchi, and T. Ishikawa, "Leukocyte margination at arteriole shear rate," Physiol. Rep. **2**, e12037 (2014).

[60] D. Barthès-Biesel, A. Diaz, and E. Dheni, "Effect of constitutive laws for two-dimensional membranes on flow-induced capsule deformation," J. Fluid. Mech. **460**, 211–222 (2002).

[61] J. Li, M. Dao, C. T. Lim, and S. Suresh, "Spectrin-level modeling of the cytoskeleton and optical tweezers stretching of the erythrocyte," Phys. Fluids **88**, 3707–6719 (2005).

[62] M. Puig-de-Morales-Marinkovic, K. T. Turner, J. P. Butler, J. J. Fredberg, and S. Suresh, "Viscoelasticity of the human red blood cell," Am. J. Physiol. Cell Physiol. **293**, C597–C605 (2007).

[63] C. Pozrikidis, "Computational hydrodynamics of capsules and biological cell," (CRC Press, London, 2010) Chap. 6 Dissipative particle dynamics modeling of red blood cells, Subsec. Appendix, pp. 213–215.

[64] G. Tomaiuolo, "Biomechanical properties of red blood cells in health and disease towards microfluidics," Biomicrofluidics **8**, 051501 (2014).

[65] J. Harkness and R. B. Whittington, "Blood-plasma viscosity: an approximate temperature-invariant arising from generalised concepts," Biorheology **6**, 169–187 (1970).

[66] S. Chen and G. D. Doolen, "Lattice boltzmann method for fluid flow," Annu. Rev. Fluid Mech. **30**, 329–364 (1998).

[67] M. M. Dupin, I. Halliday, C. M. Care, L. Alboul, and L. L. Munn, "Modeling the flow of dense suspensions of deformable particles in three dimensions," Phys. Rev. E **75**, 066707 (2007).

[68] P. L. Bhatnagar, E. P. Gross, and M. Krook, "A model for collision processes in gases. I. Small amplitude processes in charged and neutral one-component systems," Phys. Rev. **94**, 511–525 (1954).

[69] K. Yokoi, "Efficient implementation of THINC scheme: a simple and practical smoothed VOF algorithm," J. Comput. Phys. **226**, 1985–2002 (2007).

[70] S. O. Unverdi and G. Tryggvason, "A front-tracking method for viscous, incompressible, multi-fluid flows," J. Comput. Phys. **100**, 25–37 (1992).

[71] J. B. Freund, "Leukocyte margination in a model microvessel," Phys. Fluids **19**, 023301 (2007).

[72] N. Takeishi, H. Yamashita, T. Omori, N. Yokoyama, S. Wada, and M. Sugihara-Seki, "Inertial migration of red blood cells under a newtonian fluid in a circular channel," J. Fluid Mech. **952**, A35 (2022).

[73] S. Ramanujan and C. Pozrikidis, "Deformation of liquid capsules enclosed by elastic membranes in simple shear flow: large deformations and the effect of fluid viscosities," J. Fluid Mech. **361**, 117–143 (1998).

[74] D. Barthès-Biesel and H. Sgaier, "Role of membrane viscosity in the orientation and deformation of a spherical capsule suspended in shear flow," J. Fluid. Mech. **160**, 119–135 (1985).

[75] C. Pozrikidis, "Boundary integral and singularity methods for linearized viscous flow," (Cambridge University Press, Cambridge, 1992) Chap. 2 The boundary integral equations, Subsec. 2.5 Applications to particulate flows, pp. 45–58.

[76] G. B. Thurston, "Viscoelasticity of human blood," Biophys. J. **12**, 1205–1217 (1972).

[77] M. Frigo and S. G. Johnson, "The design and implementation of FFTW3," Proceedings IEEE **93**, 216–231 (2005).

[78] O. Maklad and R. J. Poole, "A review of the second normal-stress difference; its importance in various flows, measurement techniques, results for various complex fluids and theoretical predictions," J. Non-Newtoninan Fluid Mech. **292**, 104522 (2021).

[79] R. B. Bird, R. C. Armstrong, and O. Hassager, "Dynamics of Polymeric Liquids," (Wiley-Interscience, 1987) Chap. 7 Differential Constitutitve

Equations, Subsec. 7.3 Nonlinear Differential Models, pp. 350–369.

[80] A. Mujumdar, A. N. Beris, and A. B. Metzner, "Transient phenomena in thixotropic systems," J. Non-Newtonian Fluid Mech. **102**, 157–178 (2002).

[81] Y. S. Lee and N. J. Wagner, "Dynamic properties of shear thickening colloidal suspensions," Rheol. Acta **42**, 199–208 (2003).

[82] L. F. Chiara, M. E. Rosti, F. Picano, and L. Brandt, "Suspensions of deformable particles in Poiseuille flows at finite inertia," Fluid Dyn. Rese. **52**, 065507 (2020).

[83] N. Takeishi, H. Ito, M. Kaneko, and S. Wada, "Deformation of a red blood cell in a narrow rectangular microchannel," Micromachines **10**, 199 (2019).

[84] T. Omori, T. Ishikawa, D. B.-B. A.-V. Salsac, Y. Imai, and T. Yamaguchi, "Tension of red blood cell membrane in simple shear flow," Phys. Rev. E **86**, 056321 (2012).

[85] S. Suresh, J. Spatz, J. P. Mills, A. Micoulet, M. Dao, C. T. Lim, M. Beil, and T. Surfferlein, "Connections between single-cell biomechanics and human diseases states: gastrointestinal cancer and malaria," Acta Biomater. **1**, 15–30 (2005).

[86] G. Bao and S. Suresh, "Cell and molecular mechanics of biological materials," Nat. Materials. **2**, 715–725 (2003).

[87] G. G. Stokes, "On the effects of internal friction of fluids on the motion of pendulums," Trans. Camb. Phil. Soc. **9**, 1–99 (1851).